LLE Review

Quarterly Report

UR
LLE

About the Cover:

The OMEGA Laser Facility Control Room has five consoles staffed for shot operations. Middle photo: The Shot Director coordinates the overall facility operation and subsystem operators. Top left: The Beamline Operator's station, manned by the Beamline Operator and the UV-Alignment/Laser Technician for intrashot laser alignment and laser performance analysis. Top right: The Power Conditioning Operator controls the laser amplifier power supplies. Bottom right: The Laser Driver Operator controls the initial light pulse that eventually propagates down the 60 beamlines. Bottom left: The hub of Experimental Operations, where the operator positions a spherical target (seen on the right two monitors).

LLE Review

UR
LLE

Quarterly Report

Contents

In Brief

This volume of the LLE Review, covering the period April–June 1996, contains articles detailing several nonlinear processes associated with lasers and their use, as well as an article describing the computer control systems necessary to maintain and operate a large laser system such as the 60-beam OMEGA laser. The specific topics discussed in this issue include stimulated scattering in laser plasmas, power exchange between interacting laser beams, charged particles interacting with a laser pulse, thermal equilibration of optically excited states, an overview of the laser control system software in OMEGA, and a technique for cancellation of the nonlinear phase accumulation in short-pulse lasers.

Highlights of the research presented in this issue are

* The findings of a series of experiments investigating the stimulated Brillouin backscattered light from long-scale-length laser plasmas. Backscattered light from future long-scale-length ICF plasmas may be significant and affect target coupling. Measurements of the time-resolved backscattered spectra are discussed and analyzed.

* The interaction of multichromatic laser beams in a nonlinear medium. As laser beams enter a hohlraum they overlap in space. The overlapping beams can interact and exchange power among themselves, changing the illumination symmetry conditions. The interaction process is studied both analytically and numerically.

* An analytical study of an electron's motion in the electromagnetic field of a circularly polarized laser pulse in a plasma. It is shown that the electron can be efficiently accelerated and easily extracted from the pulse.

* A new approach in analyzing the relationship between optical emission and absorption of complex systems. This analysis reveals the possibility of extensive lack of thermal equilibrium of the excited electronic states during emission. This is in contradiction to the assumptions of the "universal relationship" introduced by Kennard and Stepanov.

* An overview of the OMEGA laser control system software. With the upgrade of the OMEGA laser to 60 beams, manual control of the system is impossible. Virtually every movable optic in the system is motorized and under computer control. The extensive control system and its implementation are discussed in detail.

* A discussion of the technique for cancellation of the nonlinear phase distortion due to accumulated B-integral. A GaAs plate with a negative nonlinear index of refraction is used to cancel the B-integral accumulated in a regenerative amplifier. The plate is carefully chosen to offset the buildup of the nonlinear phase distortion due to accumulated B-integral. A high degree of success is achieved.

Mark D. Skeldon
Editor

Brillouin Scattering in Long-Scale-Length Laser Plasmas

The experimental study of parametric instabilities in long-scale-length laser plasmas is very important for inertial confinement fusion (ICF). Backscattered light near the incident light wavelength has been observed in many laser-plasma experiments and is generally attributed to stimulated Brillouin scattering (SBS).[1,2] Stimulated Brillouin scattering is a parametric instability in which an incident electromagnetic wave decays into another electromagnetic wave and an ion-acoustic wave.[3,4] The instability can grow over a large volume of plasma when $n_e < n_{cr}$, where n_e and n_{cr} are the electron and critical densities, respectively. (Here n_{cr} indicates the critical density for 1054-nm laser light.) Stimulated Brillouin scattering in future, long-scale-length ICF plasmas may be significant and could pose problems for efficient coupling of laser light to ICF targets.

SBS has been studied extensively in the past, both experimentally[5–9] and theoretically.[4,10,11] At the present time, there is little or no agreement between observed SBS reflectivities and theoretical predictions based on the assumption that SBS grows convectively from thermal noise fluctuations.[12,13]

We present here a series of 1054-nm interaction experiments on Brillouin scattering carried out on long-scale-length laser plasmas produced with the 24-beam OMEGA laser facility at the Laboratory for Laser Energetics, which has subsequently been upgraded to a 60-beam, 45-kJ at 351-nm laser. We have observed time-resolved Brillouin spectra and measured the total backscattered energy. We attempt to explain these data on the basis of existing SBS theory in inhomogeneous plasmas, hydrodynamic simulations of the background plasma, and statistically described intensity distributions of the interaction beam. An important result is that the plasma-density-gradient scale length $L_n = n_e (dn_e/dx)^{-1}$, after the foil burns through, approaches that expected in proposed ICF targets ($L_n \sim 1$ mm).

In the following sections we describe the experimental arrangement (geometry, target conditions, and measurement techniques), present the experimental data, discuss the numeri-cal SBS calculations, and finally, give a detailed comparison of experimental data and calculated results.

Experimental Description

The long-scale-length, preformed plasma of these experiments was produced by exploding mass-limited CH foil targets of 6-μm thickness and 600-μm diameter overcoated with 500 Å of Al. The geometry of the experiment showing the beams and diagnostics is shown in Fig. 67.1.[5,6] Eight primary beams peaking at time 1.0 ns were followed by eight secondary beams (Fig. 67.2), peaking at 1.6 ns (i.e., delayed by 0.6 ns from the primary beams) to maintain the electron temperature $T_e > 1$ keV over a time period of 0.5 ns. The primary and secondary beams ($\lambda = 351$ nm) had an on-target energy of ~50 to 60 J each with a pulse duration of ~0.6 ns. All beams were outfitted with distributed phase plates (DPP, element size = 1.25 mm) producing a minimum spot size at the best focus of 163-μm FWHM. All beams were defocused to ~450-μm FWHM to illuminate the target uniformly with an intensity of ~5×10^{13} W/cm^2 per beam. More detailed information about the production and characterization of the background plasma and its properties can be found in Ref. 6.

The preformed plasma was then irradiated by one of the OMEGA beams at $\lambda_0 = 1054$ nm with on-target energy of ~50 J in a pulse width of 0.7-ns FWHM. This interaction beam was incident on the target at ~60° with respect to the target normal. The timing between the beginning of the heating beams and the peak of the interaction beam was varied between 2.2 and 3.7 ns (see Fig. 67.2) to access different plasma conditions. The interaction beam was propagated through a phase plate with 3-mm cells to produce a focal spot of 210-μm FWHM, giving a maximum intensity on target, averaged over many DPP speckles, of ~1.3×10^{14} W/cm^2. At the time of the peak of the earliest interaction beam (2.2 ns), the produced target plasma had a center density of 1 to 2×10^{21} cm^{-3}, which was maintained within a factor of 2 at $T_e \sim 1$ keV for approximately 1 ns. The corresponding density-gradient scale length was typically of the order of 1 mm for all timings.
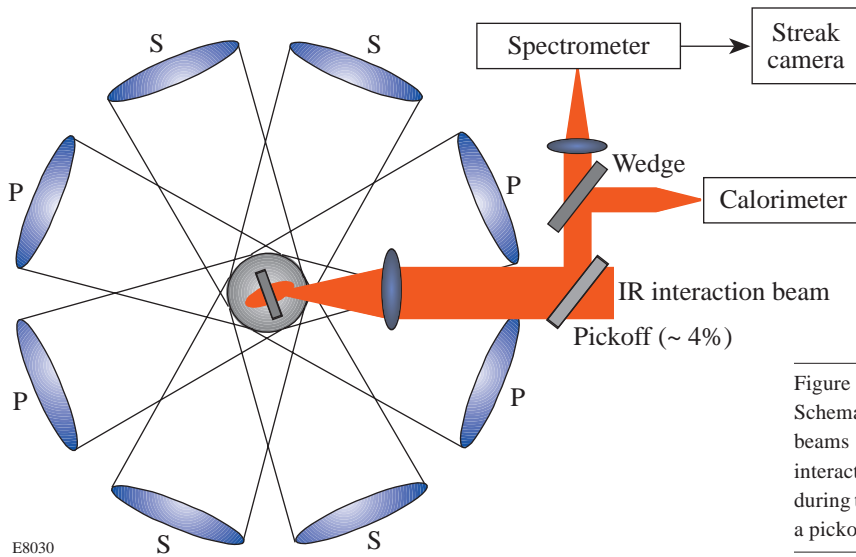
E8030

Figure 67.1
Schematic arrangement of the SBS experiments. Eight primary beams (P) are followed by eight secondary beams (S). The IR interaction beam is delayed to vary the specific plasma conditions during the interaction time. The backscattered signal is directed by a pickoff into a spectrometer/streak camera and a calorimeter.
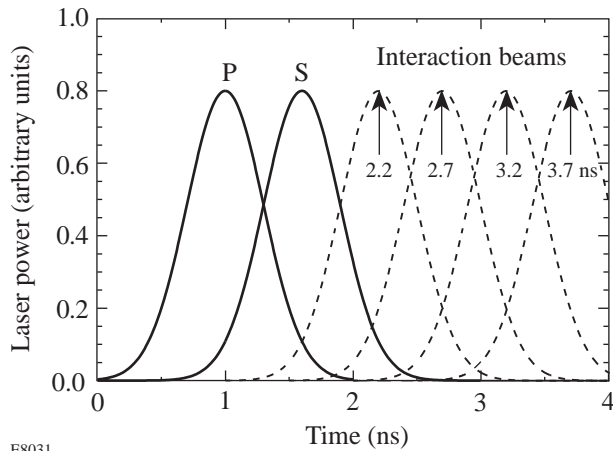

E8031

Figure 67.2
Relative timing of the primary (P), secondary (S), and interaction beams. The peak of the intensity envelope of the primary and secondary UV beams is around 2×10^{13} W/cm^2 averaged over many DPP speckles, while the peak of the intensity envelope of the interaction beam is 1.3×10^{14} W/cm^2 (also averaged over many speckles). The timing of the peak of the interaction beam was varied between 2.2 and 3.7 ns in 0.5-ns increments.

The primary diagnostic for the scattered light near λ_0 consisted of a 1-m grating SPEX spectrometer coupled to an optical streak camera (see Fig. 67.1). The backscattered light was directed by an uncoated pickoff through the lens into the spectrometer and streak camera with 5-Å spectral resolution and 30-ps time resolution, respectively. The streak camera data was recorded on film and photodensitometered for the subsequent analysis. An RG1000 filter was used to protect the

streak camera against 527- and 351-nm laser light. A set of neutral density filters was installed in front of the spectrometer slit to attenuate reflected light. Part of the reflected beam was used to measure the total energy of the backscattered light within the focusing cone of the interaction beam, using an IR calorimeter (Fig. 67.1).

Experimental Results

Typical time-resolved backscattered spectra are shown in Fig. 67.3 for three different timings τ_d of the interaction beam (2.2, 2.7, and 3.2 ns). The interaction intensity averaged over many DPP speckles was about 1.3×10^{14} W/cm^2. The time delay provides a flexible way to vary the plasma conditions seen by the interaction beam. Backscattered spectra show a few general features. First, the backscattered light is primarily blue-shifted with respect to the incident wavelength λ_0. Second, all spectra shift to shorter wavelengths with time. The width of the spectrum is typically $\Delta\omega/\omega_0 \sim 0.01$, and the total emission basically lasts up to 600 ps for all timings.

Figure 67.3(a) shows the backscattered spectrum for a timing of 2.2 ns. The width of the spectrum is about 30 Å and starts 400 ps before the peak of the pulse. This spectrum has additional spectral features: a narrow, slightly blue-shifted, spectral component preceding the interaction beam peak and the presence of a weak red-shifted component. The narrow, slightly blue-shifted component is probably due to the scattered light from the secondary heating beams, which also contain residual energy at 1054 nm left over from incomplete frequency conversion.
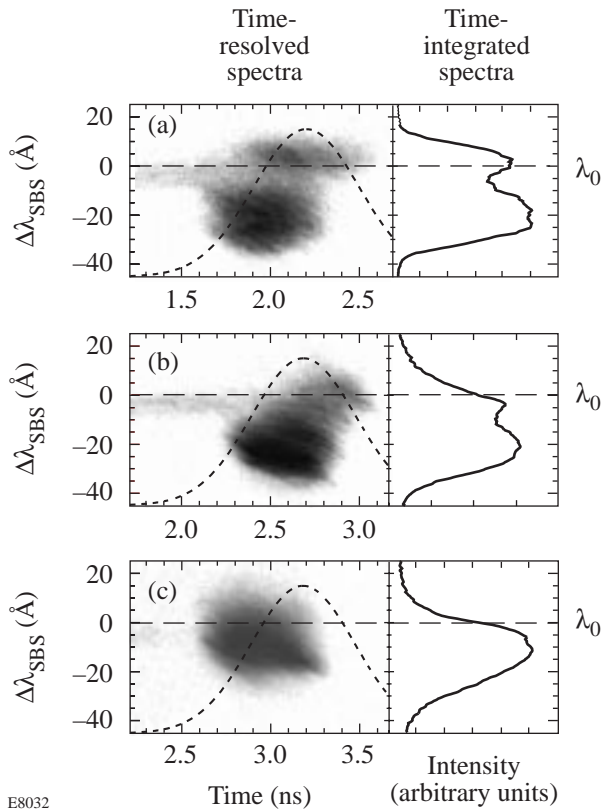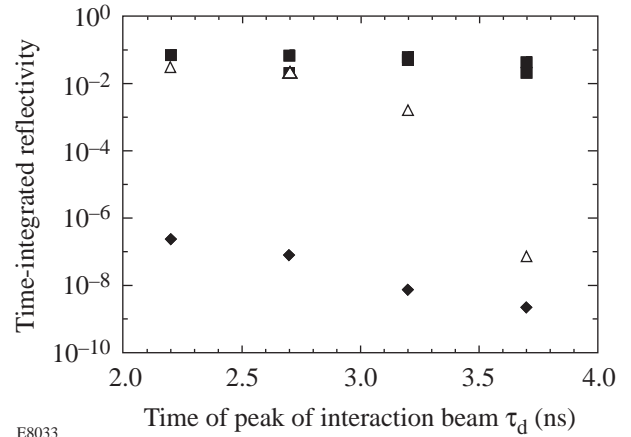
Figure 67.3

Streaked backscattered light from a CH target. The interaction beam peaks at (a) 2.2 ns, (b) 2.7 ns, and (c) 3.2 ns as indicated by the dashed curves.

A slightly red-shifted component is a feature observed only for the shortest timing of the interaction beam (2.2 ns). This component has an ~8-Å spectral width and appears later than the main blue-shifted component. The intensity of this component is about 20% less than that for the blue-shifted one. A fine spectral pattern can be noted in both components of the spectrum. This pattern is inclined to the time axis, giving the impression of lines consistently shifting toward the blue with increasing time.

The backscattered spectrum shown in Fig. 67.3(b) is for a delay of 2.7 ns. Unlike the spectrum in Fig. 67.3(a), we see mostly the blue component, which starts ~300 ps before the peak and lasts up to 600 ps. Some signal is still observed at 0 Å and the fine spectral structure becomes less visible. Finally, Fig. 67.3(c) shows the backscattered spectrum for 3.2-ns timing. It exhibits only a blue-shifted component peaked at −10 Å. The entire spectrum is less blue-shifted, starting about 400 ps before the peak and stopping 200 ps after the peak. The fine spectral structure has basically disappeared for this timing.

A plot of the measured time-integrated reflectivity of the backscattered light versus timing τ_d of the interaction beam is shown in Fig. 67.4 (solid squares). A slow decrease of Brillouin light with increased timing was observed with values between 10% for the shortest timing (2.2 ns) and 1% for the longest timing (3.7 ns). The numerical predictions indicate that the electron density n_e in the interaction region decreases from ~0.9 n_{cr} (t = 2.2 ns) to ~0.03 n_{cr} (t = 3.7 ns).

Figure 67.4

Time-integrated reflectivity R as a function of time delay of the interaction beam. Squares (■) are experimental data; triangles (△) represent the time-integrated reflectivity calculated using Eq. (7) including a hot-spot model; and diamonds (◆) show the total reflectivity based only on the peak of the intensity envelope (1.3×10^{14} W/cm²).

Theory and Simulations

In the following discussion we assume that backscattered light, at wavelengths close to that of the laser, is a consequence of the onset of the conventional SBS instability. While the resultant scattered light would be red-shifted in a quiescent plasma, our experimental plasma has supersonic flow present, which could account for the observed blue shifts. Accordingly, we calculate the scattered intensity and spectrum using conventional linear three-wave convective SBS theory.

Assuming one-dimensional (spherical) geometry, the scattered flux growing from electrostatic ion-wave thermal fluctuations (the dominant noise source) is given by a modified form of Eq. (25) in Ref. 12. For backscatter, this yields

$$F_L = \frac{cT_e}{\lambda_s^4} \frac{\omega_s}{2(\omega_0 - \omega_s)} \left[e^{G(\omega_s)} - 1 \right], \qquad (1)$$

where F_L is the flux of scattered radiation per unit solid angle per unit vacuum wavelength λ_s, and T_e is the electron temperature.

A useful expression for the gain G is given in Ref. 10. This has the form

$$G = \frac{1}{4} \int_a^b k^2 \frac{v_0^2}{c^2 |k_s|} \, \text{Im} \left[\frac{\chi_e (\chi_i + 1)}{\varepsilon(k, \omega)} \right] dx. \qquad (2)$$

Here $\mathbf{k} = \mathbf{k}_0 - \mathbf{k}_s$, $\chi_e(k, \omega)$, and $\chi_i(k, \omega)$ are the low-frequency electron and ion susceptibilities, respectively, with $\omega = \omega_0 - \omega_s$, $\varepsilon = 1 + \chi_e(k, \omega) + \chi_i(k, \omega)$, and v_0 is the peak quiver velocity $\left[v_0^2(t) \propto I(t) \right]$ of the electrons due to the inter-action beam. The wave vectors $\mathbf{k}_0$, $\mathbf{k}_s$, and $\mathbf{k}$ are the local values for the incident and scattered electromagnetic waves and the ion waves, and $c^2 k_{0,s}^2 = \omega_{0,s}^2 - \omega_{pe}^2$. The integration in Eq. (2) is taken across a finite inhomogeneous plasma from point $x = a$ at the rear of the plasma (the opposite side from the interac-tion beam) up to $x = b$, which is in the vacuum on the laser side. Both the full spectrum and the reflectivity are obtained by including all scattered frequencies. The temporal evolution of G is determined by the temporal evolution of the intensity and the plasma parameters in the interaction region. The spatial speckle distribution in the interaction beam created by the distributed phase plate can be taken into account by appropri-ate averaging of the backscattered SBS energy over the inten-sity distribution.

Application of Eq. (2) to our experiment is made by num-erical integration. The temporal evolution of the background plasma properties (plasma temperature, density, and flow velocity) is obtained from simulations using the 2-D hydrody-namic code *SAGE* in cylindrical geometry. We model the interaction beam as a finite cylinder striking the target nor-mally, while in the actual experiment the interaction beam enters at a considerable angle (~60°) to the normal. However, rapid plasma expansion, prior to the onset of the interaction beam, produces a near-spherical plasma cloud that justifies our simplified modeling.

A typical result of this *SAGE* simulation is shown in Fig. 67.5 for time $t = 2.2$ ns (the peak of the interaction beam is also at 2.2 ns in this simulation). The values shown are along the central axis of the beam. At this time, part of the plasma is still overdense to the laser beam, the density-gradient scale length L_n is of the order of 600 μm, and the velocity-gradient scale length L_v is of the order of 400 μm. Peak densities of $n_e > n_{cr}$ are present for the shorter delays, while interaction beams with the longest delays encounter a plasma with peak densities below 0.03 n_{cr}. The interaction beam sees an electron temperature varying between $T_e \approx 0.4$ and 1.2 keV. The local Mach numbers (expansion velocities) are close to zero near the plasma center and increase to $M \approx 3$ to 3.5 at the plasma edge. The interaction beam intensity decreases smoothly with pen-etration distance, owing to inverse Bremsstrahlung, and is virtually negligible after reflection from the critical surface. It is worth pointing out that at early times the interaction beam sees only regions with supersonic flow, while later in time it will propagate through both supersonic and subsonic regions of flowing plasma.

In our numerical integration, we assumed that

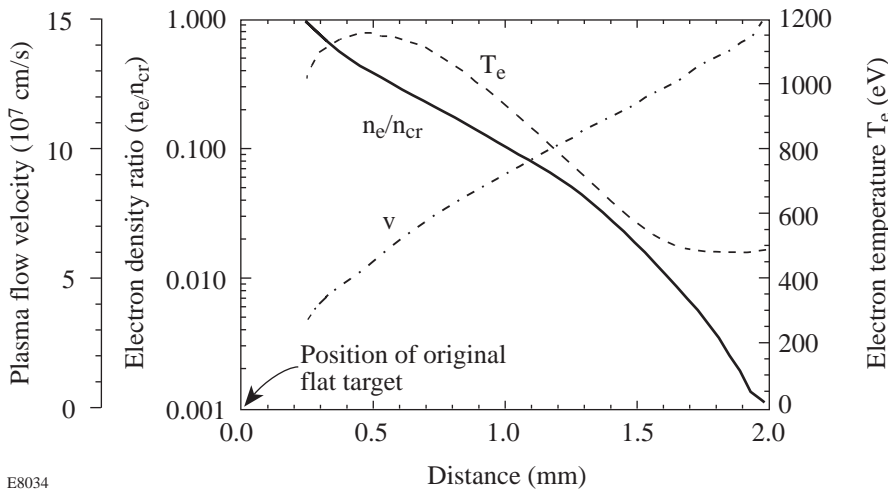$$\chi_e(k) \cong \left(k^2 \lambda_D^2 \right)^{-1} \gg 1 \qquad (3)$$

Figure 67.5
Calculated *SAGE* profiles of the relative den-sity n_e/n_{cr}, the plasma expansion velocity v, and the electron temperature T_e for a mass-limited CH target. The peak of the interaction beam is at 2.2 ns. The velocity- and density-gradient scale lengths are $L_v \approx 400$ μm and $L_n \approx 600$ μm, respectively.

E8034

and

$$\chi_i(k,\omega) \cong -\frac{\omega_{\text{pi}}^2}{(\omega - i\gamma - \mathbf{k}\cdot\mathbf{v})^2}. \qquad (4)$$

Here λ_D is the usual Debye length, ω_{pi} is the ion plasma frequency, and $\mathbf{v}$ is the plasma flow velocity. Damping has been included through the addition of an imaginary component γ to the frequency. Generally, we neglect electron Landau damping of the ion waves, and thus χ_e is real. The damping term in χ_i is chosen as a sum of the Landau damping of the ion waves and a collisional contribution. However, since the integrand in our integration over x is strongly resonant about a matching point $x_m(\lambda_s)$, where $\text{Re}[\varepsilon(x_m)] = 0$, it turns out that the resultant integral is very insensitive to the precise form chosen for γ (this is a well-known result). We have carried out additional calculations that included electron Landau damping and found only negligible corrections to our previous results.

Since G enters in an exponential in the expression for the scattered intensity, we expect a strong dependence of the total reflectivity on time delay. This is borne out by the theoretical result shown in Fig. 67.4. These solid diamonds (◆) are the calculated reflectivity based on using the average interaction intensity in the exponent. We see more than six-orders-of-magnitude difference between theory and experiment for a time delay of 3.7 ns. As the delay decreases, G increases and the theoretical curve and experimental data approach each other but still remain far apart. This major discrepancy between experiment and the conventional SBS convective theory is not new. It has been noted previously in a series of experiments covering short, intermediate, and long pulse lengths for the interaction beam.[11,13,14] It seems clear that conventional

convective SBS theory has great difficulty accounting for the measurements of backscattered radiation at frequencies close to that of the laser.

Since the intensity I appears in the exponential, we have considered whether spatial nonuniformities in the actual beam would substantially change the calculated SBS reflectivities. Inclusion of a statistical distribution of the laser-light intensity in our calculations has yielded an overall increase in G of the order of 2 or more. While this correction has a profound effect on the calculated SBS reflectivities for the shorter time delays, for which G is large (G is of the order of 10 to 20), it has little effect when G is small.

The calculation incorporating statistical nonuniformities of the actual beam was carried out as follows. From a numerical analysis of the speckles produced by the DPP at the target plane, we obtained a probability distribution of the intensity. This probability distribution and its running integral as a function of intensity are shown in Fig. 67.6. From this plot one can find the fraction of total intensity in the beam that is at or below a given intensity. This probability distribution was based on an area outlined by the FWHM (210 μm) of the distribution and containing ~50% of the total incident energy. In the actual calculations, we used an analytical fit[15] to the probability distribution:

$$P_{\text{fit}}(I) = \frac{1}{I_{\text{av}}}\exp\left(-\frac{I}{I_{\text{av}}}\right), \qquad (5)$$

where $I_{\text{av}} = 1.3 \times 10^{14}$ W/cm^2. This is a very good fit, as is shown in Fig. 67.6.
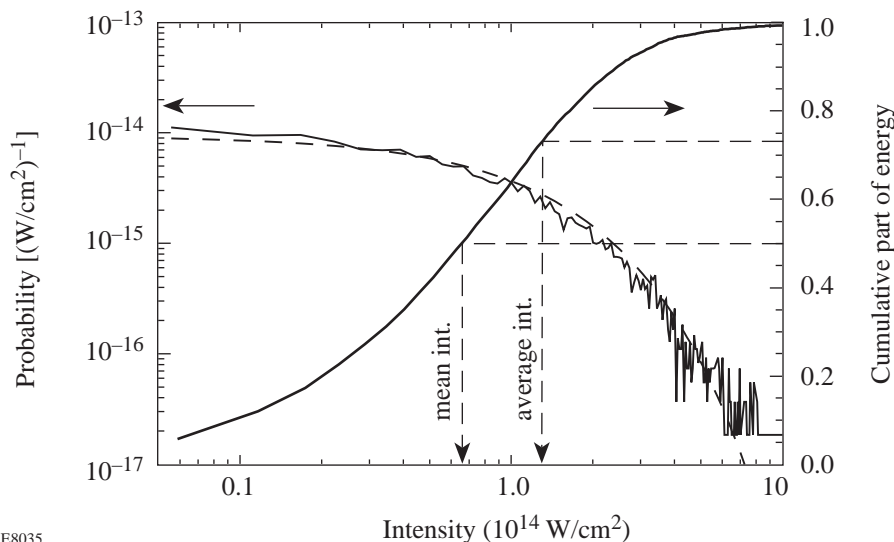

Figure 67.6
The probability distribution of the intensity of the interaction beam in the focal plane and its cumulative fraction. The dashed line shows the analytical fit given by Eq. (5).

E8035

The instantaneous flux of backscattered radiation through a solid angle $\Delta\Omega = 0.06$ sr (the solid angle subtended by the entire focusing lens) is obtained by integrating Eq. (1) over wavelength:

$$\Phi_{SBS}(I,t) = \Delta\Omega \times \int_\lambda F_L \, d\lambda. \qquad (6)$$

The time-integrated reflectivity R_{SBS} is then defined as

$$R_{SBS} \equiv \frac{E_{SBS}}{E_{in}} = \frac{\int_t \int_I \Phi_{SBS}(I,t)\, P(I,t)\, dI dt}{\int_t \int_I I(t)\, P(I,t)\, dI dt}. \qquad (7)$$

The quantities E_{SBS} and E_{in} denote the backscattered and incident energy, respectively. Using this model to calculate the reflectivity yielded the triangles ($\triangle$) shown in Fig. 67.4. For the highest gains it was necessary to include pump depletion to avoid instantaneous reflectivities of >100% for the largest intensity components.

The resultant predictions for the reflectivity are now in reasonable agreement with the experimental results for short time delays (where $n_e \sim 0.7$–$0.9\ n_{cr}$) but strongly disagree for the later timings ($n_e \le 0.03\ n_{cr}$). We found that for the shortest timings (2.2 ns) the calculated gains for the peak reflected wavelength are ~10 during the major part of the pulse. As the time delay increases, the gain decreases monotonically and becomes of the order of 1 to 2 for a delay of 3.2 ns.

While the precise dependence of G on the density and flow velocity is rather complex, we can obtain a qualitative understanding of the variation of G from an approximate analytic treatment. In the weak damping limit, there is a sharp resonance in the integrand of Eq. (2) at the resonance point, x_m, at which $\text{Re}\big[\varepsilon(x_m)\big] = 0$. Carrying out the resonant integration in x, the expression for the gain becomes[4]

$$G \cong \frac{\dfrac{\pi}{4}\left(\dfrac{v_0}{v_e}\right)^2 \dfrac{n_e}{n_c} k_0 L_v}{\left|\left(\dfrac{n_e}{n_c}\right)\left(\dfrac{L_v}{L_n}\right)(1-M) - 2M\left(1-\dfrac{n_e}{n_c}\right)\right|}, \qquad (8)$$

where M denotes the Mach number, $L_n = n_e/(dn_e/dx)$ is the density-gradient scale length, L_v is velocity-gradient scale length, and all quantities are evaluated at x_m. This result agrees exactly with the expression given in Ref. 4 if one neglects the temperature gradient (as seems appropriate for our plasma) and allows for our definition of $L_v = v(dv/dx)^{-1}$.

At the matching point, one has $\omega_0 - \omega_s - \mathbf{k}\cdot\mathbf{v} \approx kc_s$, where c_s is the sound speed, and, since $k \approx 2k_0$, this has the form $\omega_0 - \omega_s - 2\,\mathbf{k}_0\cdot\mathbf{v}(x_m) \approx 2\,kc_s$. Roughly, for a particular scattered frequency ω_s, the matching point is at a specific value of the flow velocity. As the time delay increases, we note that a given velocity moves farther out in space. The density at that point also has dropped; hence, it becomes clear why the gain decreases with increasing time delay.

The possibility that the dominant reflected beam is the phase conjugate of the laser beam has generated considerable interest. We note that phase conjugation can at most yield a factor-of-2 increase in the gain over the value obtained using the speckle-averaged intensity.[16] Once again, this will have little effect on the large discrepancy between theory and experiment for the longer time delays.

Equation (2) also allows us to predict the scattered spectrum as a function of time. If we include hot-spot variation via Eq. (5), the resultant calculated streaks (shown in Fig. 67.7) indicate reasonable agreement with the observed experimental streaks (Fig. 67.3). However, note the difference in the time variation of the calculations and the measurements. The red-shifted components seen in the calculated spectra [Figs. 67.7(b) and 67.7(c)] are due to a strong resonance in the gain integral at points close to the center of the plasma, where the expansion velocity is subsonic. With the exception of one shot, we did not see such strongly red-shifted components. This discrepancy is likely due to refraction of the interaction beam. The effect of refraction of the interaction beam is clearly seen in ray-tracing simulations carried out on the 2-D plasma profiles generated by *SAGE*. However, our simulations use only the central ray along the axis of symmetry. For such a ray, by definition, refraction does not occur. We have found no reasonable and satisfactory way to include refraction in our model since ray tracing in this region leads to caustics and crossing rays for which intensities cannot be defined without recourse to physical optics.

Since conventional SBS linear gain theory cannot account apparently for all our observations, one should note other possible explanations. Among the possibilities raised in the
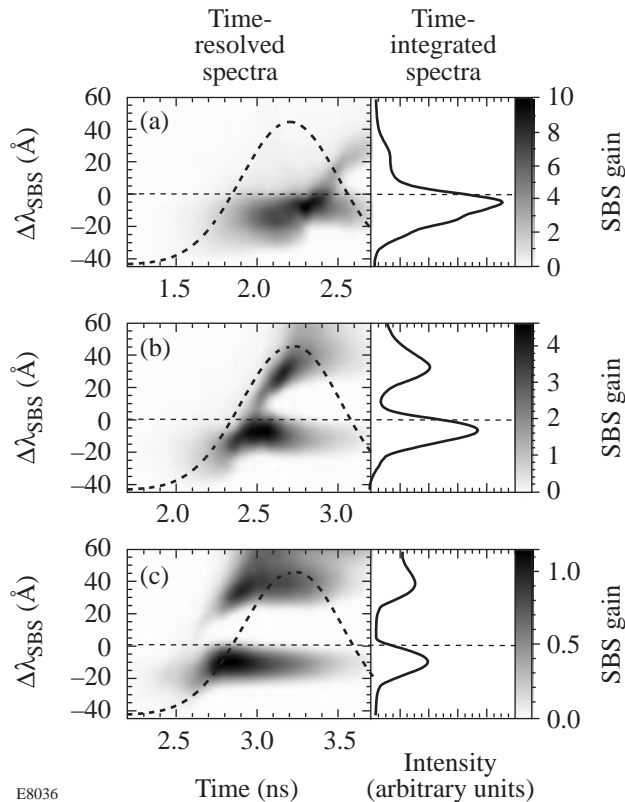
Figure 67.7
Calculated SBS gain as a function of time and spectral shift for three timings of the interaction beam: (a) 2.2 ns, (b) 2.7 ns, and (c) 3.2 ns. Hot-spot variation of the intensity is modeled using Eq. (5), and pump depletion is included.

literature, we call attention to the possible role of filamentation,[17] ion beams,[18,19] and enhanced ion wave noise.[20] In addition, one other explanation should be offered for the relative insensitivity of the SBS signal to the delay time seen in Fig. 67.4. The target is initially exploded by four primary beams from each side, which, when overlapped, produce a pattern that has four minima around the azimuth. Three-dimensional effects associated with these portions disassembling slower than average may result in the maintenance of near-critical densities for longer than predicted by the azimuthally symmetric *SAGE* calculations.

We should note also that we have examined density and velocity perturbations (ripples) that could propagate down the density gradient at the sound velocity in the flowing plasma. Assuming enhanced SBS at the top of such ripples, one can reproduce quite well the slope of the fine structure seen in Fig. 67.3(a). However, for Fig. 67.3(b) the slope of the resultant fine structure differs significantly from the observations.

Since it is also difficult to argue how such ripples lead to locally enhanced SBS reflectivities, we conclude that this mechanism is unlikely to account for the observed spectral fine structure.

Summary and Conclusions

We have observed backscattered Brillouin spectra for a range of interaction beam delays corresponding to electron-density changes during the interaction pulse. The blue-shifted spectra of the reflected light are centered mostly near −15 Å. The spectra for the shortest timings also include a slightly red-shifted component. The measured backscattered light reflectivity is in the range of 1%–7%. Calculated SBS reflectivities are in agreement with the measurements for the shortest timings (plasma densities near critical) but are far below the experimental reflectivities for the later timings ($n_e < 0.1\ n_{cr}$). Calculations of the spectra yield a blue shift similar to the observations, but the predicted and observed time variations differ. A calculated red-shifted component is generally not observed in the experiments, a discrepancy that is attributed to refraction of the interaction beam, which is not included in the calculations.

REFERENCES

1. P. E. Young, H. A. Baldis, and K. G. Estabrook, Phys. Fluids B **3**, 1245 (1991).

2. H. A. Baldis *et al.*, in *Femtosecond to Nanosecond High-Intensity Lasers and Applications*, edited by E. M. Campbell (SPIE, Bellingham, WA, 1990), Vol. 1229, pp. 144–149.

3. M. N. Rosenbluth, Phys. Rev. Lett. **29**, 565 (1972).

4. C. S. Liu, M. N. Rosenbluth, and R. B. White, Phys. Fluids **17**, 1211 (1974).

5. W. Seka, R. S. Craxton, R. E. Bahr, D. L. Brown, D. K. Bradley, P. A. Jaanimagi, B. Yaakobi, and R. Epstein, Phys. Fluids B **4**, 432 (1992).

6. W. Seka, R. E. Bahr, R. W. Short, A. Simon, R. S. Craxton, D. S. Montgomery, and A. E. Rubenchik, Phys. Fluids B **4**, 2232 (1992).

7. H. A. Baldis, E. M. Campbell, and W. L. Kruer, in *Handbook of Plasma Physics*, Physics of Laser Plasma, edited by A. Rubenchik and S. Witkowski (North-Holland, Amsterdam, 1991), Vol. 3, pp. 361–434.

8. R. P. Drake *et al*., Phys. Fluids **31**, 1795 (1988).

9. D. R. Gray *et al*., Plasma Physics **22**, 967 (1980).

10. G. R. Mitchel, T. W. Johnston, and H. Pépin, Phys. Fluids **26**, 2292 (1983).

11. H. A. Baldis *et al*., Phys. Fluids B **5**, 3319 (1993).

12. R. L. Berger, E. A. Williams, and A. Simon, Phys. Fluids B **1**, 414 (1989). Note that Eq. (25) has an obvious misprint; however, it simplifies even further. The derivation carried out in that paper neglected the *x*-dependence of the group velocity v_{gs}. If this is included, a revised form of Eq. (25) results in which the last bracket is replaced simply by cos Θ. For backscatter, this reduces to our Eq. (1).

13. P. E. Young *et al*., Phys. Fluids B **2**, 1907 (1990).

14. H. A. Baldis *et al*., Lawrence Livermore National Laboratory Inertial Confinement Fusion ICF Quarterly Report UCRL-LR-105821-93-3, 1993 (unpublished), p. 137.

15. H. A. Rose and D. F. DuBois, Phys. Fluids B **5**, 590 (1993).

16. B. Ya. Zel'dovich, N. F. Pilipetsky, and V. V. Shkunov, in *Principles of Phase Conjugation,* Springer Series in Optical Sciences, edited by J. M. Enoch *et al.* (Springer-Verlag, Berlin, 1985), Vol. 42.

17. J. D. Moody *et al*., Phys. Plasmas **2**, 4285 (1995).

18. A. Simon, Bull. Am. Phys. Soc. **38**, 1935 (1993).

19. A. Simon, Bull. Am. Phys. Soc. **40**, 1779 (1995).

20. S. D. Baton *et al*., Phys. Rev. E **49**, R3602 (1994).

Power Exchange between Crossed Laser Beams and the Associated Frequency Cascade

Stimulated Brillouin scattering (SBS) in a plasma[1] is the decay of a higher-frequency light wave into a lower-frequency light wave and an ion-acoustic wave. There is considerable current interest in the near-forward SBS of one[2,3] and two[4–6] laser beams because of its relevance to inertial confinement fusion (ICF) research.[7,8]

The indirect-drive approach to ICF[8] involves multichromatic laser beams that overlap as they enter the hohlraum. SBS allows the frequency components of one beam to interact with the frequency components of another beam. Because a power transfer between the beams affects the implosion symmetry adversely, it is important to understand this process.

Consider the interaction of two crossed laser beams (A and B) that have a common carrier frequency ω_0. The ponderomotive force associated with the beams drives an ion-acoustic (sound) wave (grating) of wave vector $\mathbf{k}_s = \mathbf{k}_a - \mathbf{k}_b$ and frequency $\omega_s = c_s k_s$, as shown in Fig. 67.8(a). In turn, the grating scatters the laser light from one beam direction to the other. This interaction is governed by the equations[3,6]

$$\partial_\xi A = -i\left(\omega_e^2/2\omega_0 c\right)nB,$$
$$\partial_\eta B = -i\left(\omega_e^2/2\omega_0 c\right)n * A, \tag{1}$$

and

$$\left(\partial_{tt}^2 + 2\nu_s\partial_t + \omega_s^2\right)n = -\omega_s^2 AB*, \tag{2}$$

where $A = \left(v_a/c_s\right)\left(m_e/m_i\right)^{1/2}$ and $B = \left(v_b/c_s\right)\left(m_e/m_i\right)^{1/2}$ are the electron quiver velocities associated with the laser fields divided by a characteristic speed that is of the order of the electron thermal speed and n is the electron-density variation associated with the grating divided by the background electron density. In Eq. (1), ξ and η represent distance measured along the propagation directions of the beams, as shown in Fig. 67.8(b). The time derivatives were omitted from Eqs. (1) because the time taken by the beams to cross the interaction region is much shorter than the time taken by the grating to respond to the ponderomotive force.

Previous studies of the interaction of two crossed laser beams[4–6] assumed that the beams were monochromatic. If the beam frequencies are equal, there is no power transfer in steady state. Conversely, if the beam frequencies differ, in steady state there is a monotonic transfer of power from the higher-frequency beam to the lower-frequency beam.

In this article we allow the beams to have many frequency components and study the power transfer between the beams
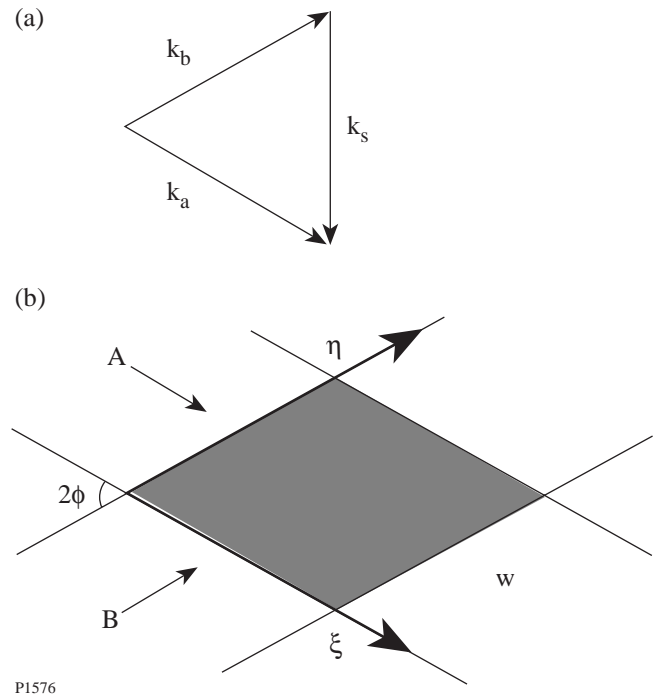

Figure 67.8
Geometry of the interaction of crossed laser beams. (a) Wave vectors of the laser beams and the ion-acoustic wave. (b) The beam widths are equal and denoted by w; the beam intersection angle is denoted by 2ϕ. The characteristic coordinates ξ and η measure distance in the propagation direction of beam A and B, respectively.

and the associated frequency cascade. For simplicity suppose that each beam has two frequency components with a frequency separation equal to the sound frequency. Subsequently, other frequency components are generated by the interaction, with the same frequency separation that was present initially. One can highlight this frequency cascade by writing

$$A = \sum_j A_j \exp\left(-i\omega_j t\right),$$

$$B = \sum_j B_j \exp\left(-i\omega_j t\right),$$

(3)

where $\omega_j = j\omega_s$ and

$$n = M \exp\left(-i\omega_s t\right) + N \exp\left(i\omega_s t\right).$$

(4)

By substituting definitions (3) and (4) in Eqs. (1) and (2), and making the substitutions

$$A_j / I^{1/2} \to A_j, \quad B_j / I^{1/2} \to B_j,$$

$$\left(2\omega_s v_s / \omega_s^2 I\right)M \to M, \quad \left(2\omega_s v_s / \omega_s^2 I\right)N \to N,$$

$$\gamma\xi \to \xi, \quad \text{and} \quad \gamma\eta \to \eta,$$

where I is the intensity of beam A as it enters the interaction region and $\gamma = \omega_e^2 \omega_s^2 I / 4\omega_0 \omega_s v_s c$ is the spatial growth rate of SBS, one can show that

$$d_\xi A_j = -i\left(M B_{j-1} + N B_{j+1}\right),$$

$$d_\eta B_j = -i\left(N * A_{j-1} + M * A_{j+1}\right),$$

(5)

where

$$M = -i\sum_j A_j B_{j-1}^*,$$

$$N = i\sum_j A_j B_{j+1}^*.$$

(6)

The distance variables ξ and η range from 0 to l, where l is the number of SBS gain lengths over which the interaction occurs. The dependence of l on the beam and plasma parameters is discussed in detail in Refs. 4 and 6. In recent simulations[4] and experiments[9] relevant to ICF, the idealized values of l were 10 and 20, respectively. Although small-scale inhomogeneities of the beams and plasma can reduce the value of

l in experiments,[9] it is potentially large enough to warrant a detailed study of crossed-beam interactions in ICF.

Because of the intrinsic complexity of the frequency cascade, we began our study with the one-dimensional (1-D) equations

$$d_x A_j = -i\left(M B_{j-1} + N B_{j+1}\right),$$

$$d_x B_j = -i\left(N * A_{j-1} + M * A_{j+1}\right),$$

(7)

where x represents distance measured along a line that bisects the angle between the ξ and η axes. The 1-D cascade Eqs. (6) and (7) are generalizations of equations that arise in the study of the beat-wave accelerator.[10,11]

A truncated set of 1-D cascade equations that allow each beam to have 20 frequency components was solved numerically, subject to the boundary conditions $A_1(0) = A_0(0) = 1$ and $B_1(0) = B_0(0) = \rho$. The intensities of the first ten frequency components of each beam, at discrete distances from the boundary, are displayed in Figs. 67.9 and 67.10 for the case in which $\rho = 0.3$. Although the "microscopic" evolution of the individual frequency components is complicated, certain trends are evident in the figures; most of the power contained in beam A is transferred to beam B, then returned to beam A. As power is exchanged, the average frequencies of the beam spectra decrease and the range of frequencies over which power is distributed increases.

Motivated by the apparent periodicity of the power exchange, we plotted the total beam intensities

$$P = \sum_j \left|A_j\right|^2, \quad Q = \sum_j \left|B_j\right|^2$$

(8)

and the grating strengths

$$R = |M|^2, \quad S = |N|^2$$

(9)

as functions of distance. The evolution of these "macroscopic" quantities is displayed in Fig. 67.11 for the case in which $\rho = 0.3$. Despite the complexity of the microscopic evolution, the macroscopic evolution is periodic and predictable! To test the robustness of the observed periodicity, the 1-D cascade equations were solved numerically for boundary conditions that included phase shifts between the beams (complex ρ) and between the frequency components of each beam. In all
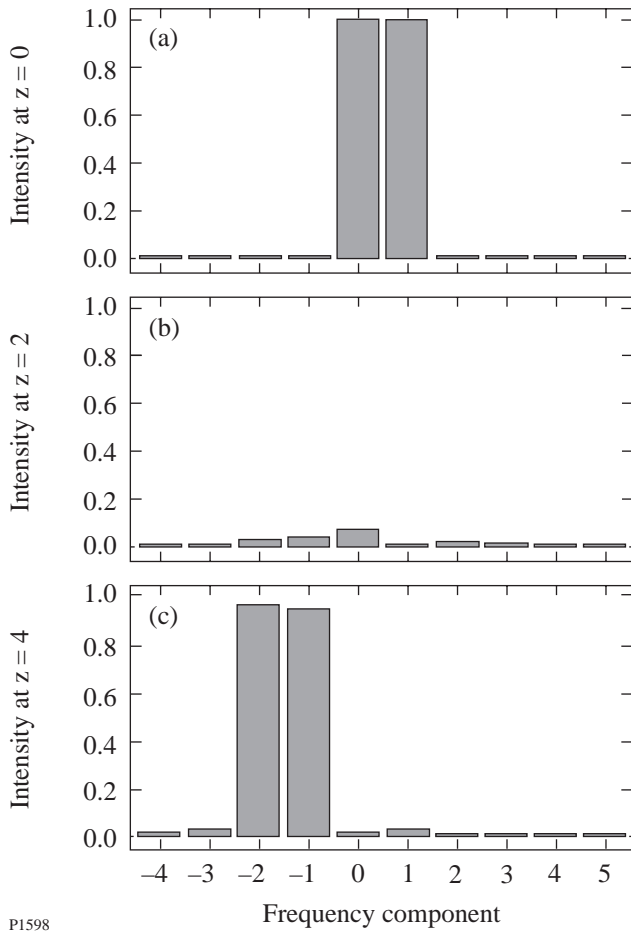
Figure 67.9
Frequency spectra of beam A obtained by solving the 1-D cascade Eqs. (6) and (7) numerically.

Figure 67.10
Frequency spectra of beam B obtained by solving the 1-D cascade Eqs. (6) and (7) numerically.

cases the macroscopic evolution was unchanged. This result prompted an analytic analysis of the macroscopic evolution.
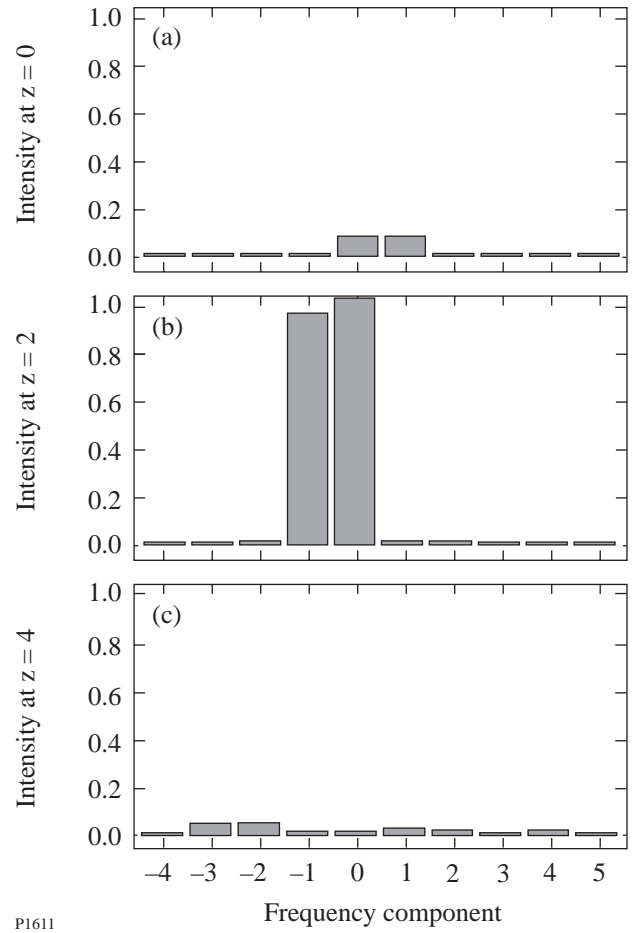
It follows from the 1-D cascade equations that

$$d_x P = -2(R - S), \quad d_x Q = 2(R - S) \qquad (10)$$

and

$$d_x R = 2R(P - Q), \quad d_x S = -2S(P - Q). \qquad (11)$$

Equations (10) are valid for arbitrary boundary conditions on beams A and B. Terms were omitted from Eqs. (11) that equal zero for the boundary conditions described between Eqs. (7) and (8). There are three conservation laws associated with these model equations. The first is $P + Q = T$, where $T = 2 + 2r$ is the sum of the initial beam intensities. The second is

$R + S = U + TQ - Q^2$, where $U = -2r'$, and the third is $RS = V$, where $V = r^2$ is the product of the initial grating strengths. By using these conservation laws, one can eliminate R, S, and P from the model equations, which reduce to the potential equation

$$(d_x Q)^2 = 4Q(Q - 2r)(Q - 2)(Q - 2 - 2r). \qquad (12)$$

It follows immediately that Q oscillates regularly between $2r$, the initial intensity of beam B, and 2, the initial intensity of beam A. As a bonus, Eq. (12) can be solved analytically.[12] The result is

$$Q(x) = \frac{2r}{1 - (1 - r)\mathrm{sn}^2(2x, m)}, \qquad (13)$$

where $\mathrm{sn}(2x, m)$ is the elliptic sine function of argument $2x$
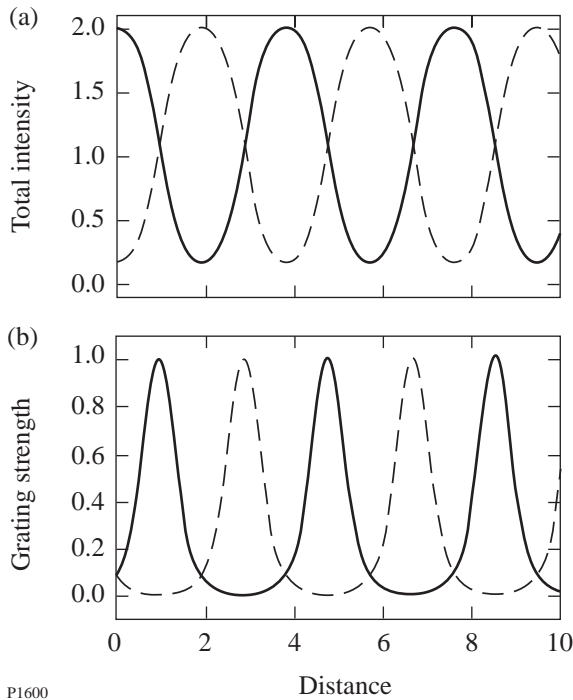
(a)

(b)

P1600

Figure 67.11
Periodic evolution of (a) the beam intensities P (solid line) and Q (broken line), and (b) the grating strengths R (solid line) and S (broken line) obtained by solving the 1-D cascade Eqs. (6) and (7) numerically.

and order $m = 1 - r^2$. Solution (13) is compared to the numerical solution of the 1-D cascade equations in Fig. 67.12. The agreement is excellent. It follows from solution (13) that the spatial period of the power exchange

$$l = K(m), \qquad (14)$$

where $K(m)$ is the complete elliptic integral of the first kind. For an initial intensity ratio $r = 0.09$, $l \approx 3.8$, in agreement with Fig. 67.12. One can obtain the same result by using the simpler formula $l \approx \log(4/r)$, which is valid for $r \ll 1$.

In contrast to monochromatic illumination, which results in a monotonic transfer of power from one beam to the other, multichromatic illumination results in a periodic exchange of power between the beams. The main difference between the two cases is the presence of grating N in the latter, which allows energy to be transferred from the higher-frequency components of beam B to the lower-frequency components of beam A. This assertion is supported by Fig. 67.11(b), in which the growth of grating N after beam A has been depleted is a precursor to the transfer of energy from beam B back to beam A.
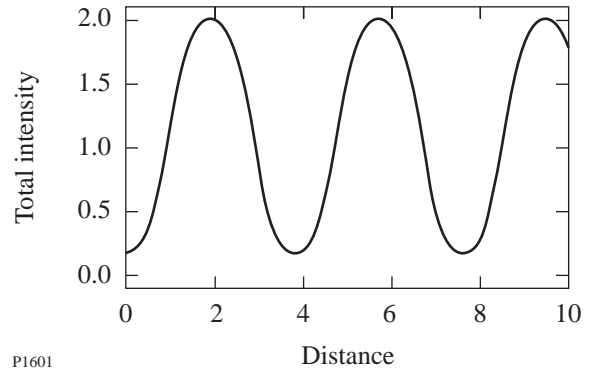

P1601

Figure 67.12
Comparison of the evolution of the intensity of beam B predicted by the 1-D cascade Eqs. (6) and (7) and the potential Eq. (12). The two results are visually indistinguishable.

To test the validity of the preceding 1-D results, we integrated the two-dimensional (2-D) cascade Eqs. (5) and (6) numerically, subject to boundary conditions that are the 2-D analogs of those described between Eqs. (7) and (8). When the beams intersect as they enter the plasma, the interaction region is a triangle. When the beams intersect after they have entered the plasma, the interaction region is a rhombus.

The results for the triangular interaction region are displayed in Fig. 67.13. Light shading represents high beam intensity and grating strength, whereas dark shading represents low beam intensity and grating strength. The beam and grating evolution is periodic in the x direction, and the growth of grating N is a precursor to the transfer of power from beam B back to beam A, as predicted by the 1-D cascade equations. Within the interaction region, the 1-D and 2-D results agree quantitatively.

The results for the rhomboidal interaction region are displayed in Fig. 67.14. Clearly, the beam evolution is not periodic in any direction. Although 2-D rhomboidal geometry suppresses the periodicity that is characteristic of the 1-D and 2-D triangular geometries, it does not suppress the effects of multichromatic illumination completely. Under monochromatic illumination $p(a, s, 0) = \exp(-2r\xi)$: the intensity of beam A decreases as it propagates near the entry boundary of beam B, as shown in Fig. 66.33 of LLE Review 66 (see Ref. 6). In contrast, under multichromatic illumination $p(\xi, 0) = 1 + \cosh(4r\xi)$: the intensity of beam A increases slowly as it propagates near this boundary, as shown in Fig. 67.14(a). Once again this qualitative difference is due to grating N, which is strong near the aforementioned boundary, as shown in Fig. 67.14(b).
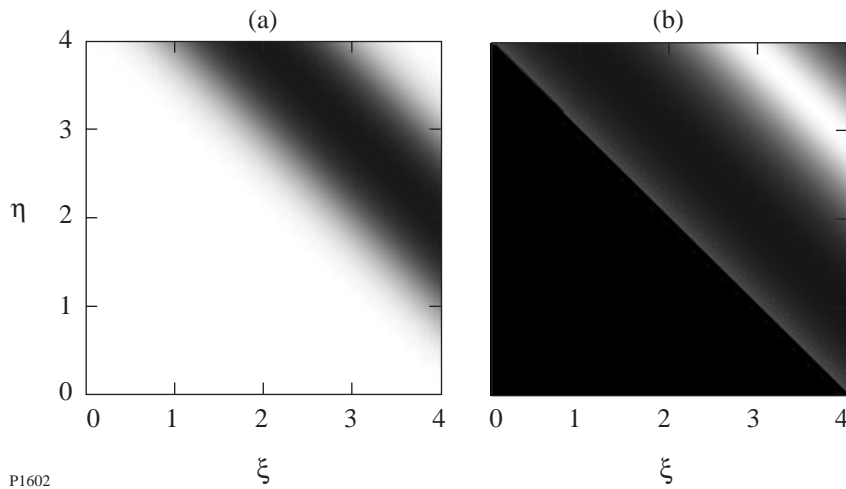
130

Figure 67.13
Grayscale plot of (a) the total intensity of beam A and (b) the strength of grating N obtained by solving the 2-D cascade Eqs. (5) and (6) numerically for a triangular interaction region. The horizontal and vertical axes correspond to the propagation directions of beams A and B, respectively.
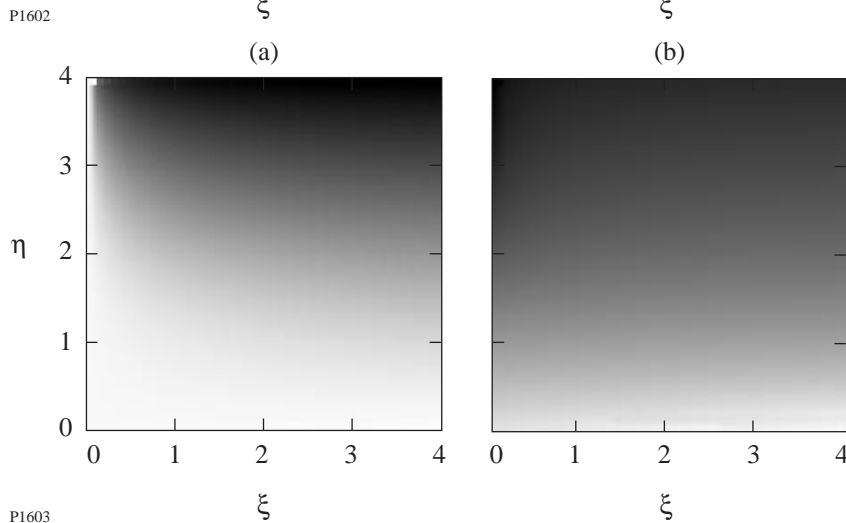
P1602

Figure 67.14
Grayscale plot of (a) the total intensity of beam A and (b) the strength of grating N obtained by solving the 2-D cascade Eqs. (5) and (6) numerically for a rhomboidal interaction region. The horizontal and vertical axes correspond to the propagation directions of beams A and B, respectively.

P1603

In summary, the power exchange between two crossed laser beams was studied analytically and numerically. Multichromatic illumination and two-dimensional geometry are both capable of changing the qualitative character of the beam evolution, so their effects should not be overlooked.

REFERENCES

1. W. L. Kruer, *The Physics of Laser Plasma Interactions* (Addison-Wesley, Redwood City, CA, 1988), Chaps. 7 and 8.

2. C. J. McKinstrie, R. Betti, R. E. Giacone, T. Kolber, and J. S. Li, Phys. Rev. E **50**, 2182 (1994).

3. R. E. Giacone, C. J. McKinstrie, and R. Betti, Phys. Plasmas **2**, 4596 (1995).

4. W. L. Kruer *et al.*, Phys. Plasmas **3**, 382 (1996).

5. V. V. Eliseev *et al.*, Phys. Plasmas **3**, 2215 (1996).

6. Laboratory for Laser Energetics LLE Review **66**, NTIS document No. DOE/SF/19460-125, 1996 (unpublished), p. 73; C. J. McKinstrie, J. S. Li, R. E. Giacone, and H. X. Vu, Phys. Plasmas **3**, 2686 (1996).

7. R. L. McCrory and J. M. Soures, in *Laser-Induced Plasmas and Applications*, edited by L. J. Radziemski and D. A. Cremers (Dekker, New York, 1989), p. 207.

8. J. D. Lindl, Phys. Plasmas **2**, 3933 (1995).

9. R. K. Kirkwood *et al.*, Phys. Rev. Lett. **76**, 2065 (1996).

10. B. I. Cohen, A. N. Kaufman, and K. M. Watson, Phys. Rev. Lett. **29**, 581 (1972).

11. S. J. Karttunen and R. R. E. Salomaa, Phys. Rev. Lett. **56**, 604 (1986).

12. C. J. McKinstrie, X. D. Cao, and J. S. Li, J. Opt. Soc. Am. B **10**, 1856 (1993), App. A.

Electron Acceleration by a Laser Pulse in a Plasma

The motion of a charged particle in an electromagnetic field is a well-known paradigm of physics.[1,2] Suppose that the field is associated with a laser pulse of finite extent propagating in a vacuum. As the pulse overtakes the particle, the particle gains energy and momentum at the expense of the pulse. At the peak of an intense pulse, the particle has considerable (longitudinal) momentum in the propagation direction of the pulse. This fact suggests that intense pulses[3] might be used to accelerate particles. Unfortunately, the energy associated with the transverse particle motion is wasted, and it is difficult to extract the particle from the middle of the pulse. One cannot simply wait until the pulse has overtaken the particle completely because the pulse leaves the particle at rest, albeit displaced a finite distance in the direction of the pulse. If the pulse is of finite transverse extent, the particle can be expelled from the pulse.[4] However, this transverse expulsion is difficult to control.

In this article, we describe the motion of a charged particle in the field of an idealized laser pulse propagating through a medium and show that the particle can be accelerated efficiently and extracted easily. We then discuss briefly some issues relevant to electron acceleration in a plasma. For a detailed review of laser-driven electron acceleration schemes, we refer the reader to the paper by Sprangle, Esarey, and Krall.[5]

The motion of a particle, of charge q and mass m, in an electromagnetic field is governed by the equation[6]

$$d_\tau\left(u_\mu + a_\mu\right) = u^\nu \partial_\mu a_\nu, \tag{1}$$

where u^μ is the four-velocity of the particle, τ is the proper time of the particle multiplied by c, and a^μ is the four-potential of the field multiplied by q/mc^2. For a circularly polarized field

$$a^\mu = \left(0, 0, a\cos\phi, a\sin\phi\right)/\sqrt{2}. \tag{2}$$

We assume that the phase ϕ and amplitude a are functions of t and x alone. In this case, it is well known that

$$d_\tau\left(\mathbf{u}_\perp + \mathbf{a}_\perp\right) = 0, \tag{3}$$

which reflects the conservation of transverse canonical momentum. For future reference, notice that Eq. (3) does not imply that $\mathbf{u}_\perp$ attains all values of $\mathbf{a}_\perp$; it implies that the values of $\mathbf{a}_\perp$ to which the particle has access are reflected in the corresponding values of $\mathbf{u}_\perp$. Using Eq. (3), one can rewrite the first two components of Eq. (1) as

$$d_\tau\gamma = \frac{1}{2}\partial_t u_\perp^2, \quad d_\tau u_\parallel = -\frac{1}{2}\partial_x u_\perp^2. \tag{4}$$

The right sides of Eqs. (4) are the t- and x-components of the ponderomotive four-force.

We assume that $\phi = t - sx$, where s is the inverse phase speed of the pulse, and $a = a(\psi)$, where $\psi = t - rx$ and the inverse pulse speed $r > 1$. Although these assumptions are based on the known characteristics of a low-intensity pulse, which may differ from those of a high-intensity pulse, the only requirements of the following analysis are that the pulse propagates without distorting significantly and that its propagation speed is less than c. The propagation characteristics of high-intensity pulses have been studied by Decker and Mori.[7]

Since $u_\perp^2$ is independent of ϕ, it follows from Eqs. (4) that

$$d_\tau\left(r\gamma - u_\parallel\right) = 0. \tag{5}$$

For a particle that is at rest initially, $u_\parallel = r(\gamma - 1)$. Since $r > 1$, longitudinal momentum is produced more efficiently in a medium than in a vacuum. By combining this result with the definition of the Lorentz factor γ, one can show that

$$\left(r^2 - 1\right)u_\parallel^2 - 2r u_\parallel + r^2 u_\perp^2 = 0. \tag{6}$$

It follows immediately that

$$u_\parallel = \frac{r \pm r\left[1 - \left(r^2 - 1\right)u_\perp^2\right]^{1/2}}{r^2 - 1} \tag{7}$$

and

$$\gamma = \frac{r^2 \pm \left[1 - \left(r^2 - 1\right)u_\perp^2\right]^{1/2}}{r^2 - 1} . \tag{8}$$

Equation (6) describes an ellipse that intersects the origin and has semi-major and semi-minor axes of length $r/\left(r^2 - 1\right)$ and $1/\left(r^2 - 1\right)^{1/2}$, respectively, as shown in Fig. 67.15. The minus (−) signs in Eqs. (7) and (8) correspond to the left half of the ellipse, whereas the plus (+) signs correspond to the right half. It follows from Eqs. (7) and (8) that $v_\parallel = 1/r$ at the intermediate point B. This information allows the particle motion to be determined qualitatively.

Initially, the pulse overtakes the particle. As it does so, $u_\perp^2$ increases and the representative point $\left(u_\parallel, |u_\perp|\right)$ moves from A, which corresponds to the leading edge of the pulse, toward B. If $u_\perp^2 < 1/\left(r^2 - 1\right)$ at the peak of the pulse, the representative point does not reach B. Since $v_\parallel < 1/r$, the pulse overtakes the

particle completely and the representative point moves back toward A, which now corresponds to the trailing edge of the pulse. Eventually, the particle is at rest. This scenario is illustrated in Fig. 67.16(a). However, if $u_\perp^2 = 1/\left(r^2 - 1\right)$ before the particle reaches the peak of the pulse, the particle is repelled by the pulse, because the *x*-component of the ponderomotive four-force is positive, and the representative point continues toward C, which corresponds to the leading edge of the pulse. Eventually, $u_\perp = 0$, $u_\parallel = 2r/\left(r^2 - 1\right)$, and $\gamma = \left(r^2 + 1\right)/\left(r^2 - 1\right)$. This scenario is illustrated in Fig. 67.16(b). The Palmer theorem[8] does not apply to this scenario because the ponderomotive terms in Eqs. (4) are nonlinear and the pulse is propagating through a medium.

During this interaction, the phase of the pulse evolves according to $d_\tau\phi = \gamma\left(1 - sv_\parallel\right)$. Initially, $d_\tau\phi = 1$ and a positively charged particle rotates in an anticlockwise direction.[9] As the particle's speed increases, its rate of rotation decreases. For media in which $r < s$, the direction in which the particle rotates can change if the pulse is sufficiently intense.

For reasons that will become clear shortly, consider the acceleration of a particle that is traveling in the direction of the pulse with initial momentum u_A and initial energy γ_A. The analysis of particle acceleration is simplest in the pulse frame, in which the four-potential is time independent and, hence, the particle energy is constant; energy is exchanged between the longitudinal and transverse degrees of freedom. Because the four-potential is transverse, it has the same amplitude in both the laboratory and pulse frames. Let $\gamma_P = r/\left(r^2 - 1\right)^{1/2}$ be the Lorentz factor associated with the pulse and $u_P = \left(\gamma_P^2 - 1\right)^{1/2}$. Initially, the particle is moving to the left in the pulse frame. The particle will be repelled if, at some point in the pulse, the energy associated with its transverse motion equals its initial energy. In this case the particle regains its initial energy as it moves to the right. It follows from these observations and Eq. (2) that, in the laboratory frame,
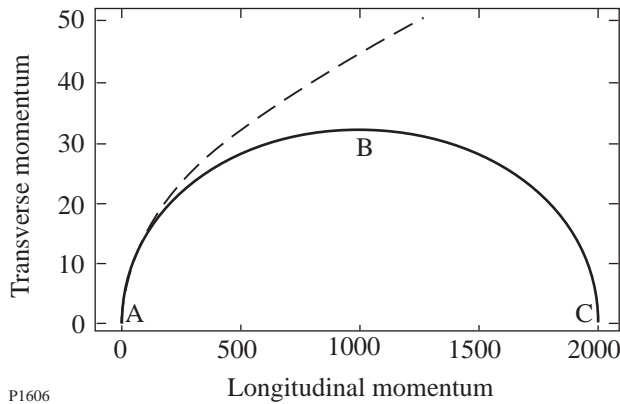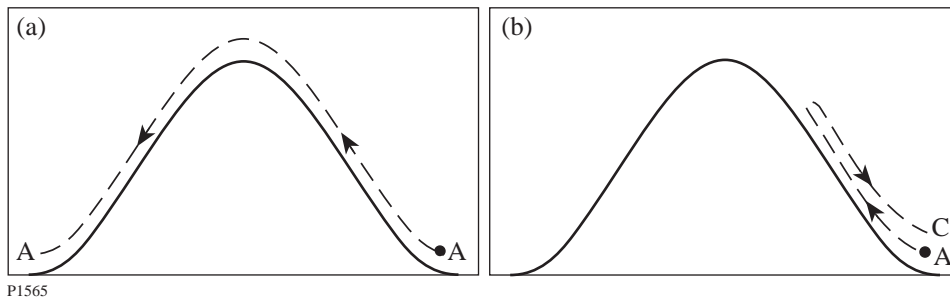

Figure 67.15
Diagram of the relation between longitudinal and transverse momentum implied by Eq. (6). The broken line corresponds to $r = 1$ (vacuum) and the solid line corresponds to $r = 1.0005$ (medium).

Figure 67.16
Illustration of the particle motion for a low-intensity pulse (a) and a high-intensity pulse (b).

the repelling threshold

$$a_B^2 = \left[(\gamma_P \gamma_A - u_P u_A)^2 - 1 \right] \qquad (9)$$

and the corresponding gain in particle energy

$$\delta\gamma = 2 \left(u_P^2 \gamma_A - \gamma_P u_P u_A \right). \qquad (10)$$

The energy gain and repelling threshold are plotted as functions of the initial energy in Fig. 67.17, for the case in which $\gamma_P = 30$. Energy is measured in units of the particle rest mass. If the particle is at rest initially, $a_B^2 = 2(\gamma_P^2 - 1) = \delta\gamma$; the energy gain is large, but so is the required pulse intensity. Since the repelling threshold decreases more rapidly than the energy gain as the initial energy is increased, the intensity requirement can be minimized by injecting preaccelerated particles. For example, if the injection energy is 7, the repelling threshold is 8.3 and the energy gain is 120. If the injection energy is 15, the repelling threshold is 1.1 and the energy gain is 45.
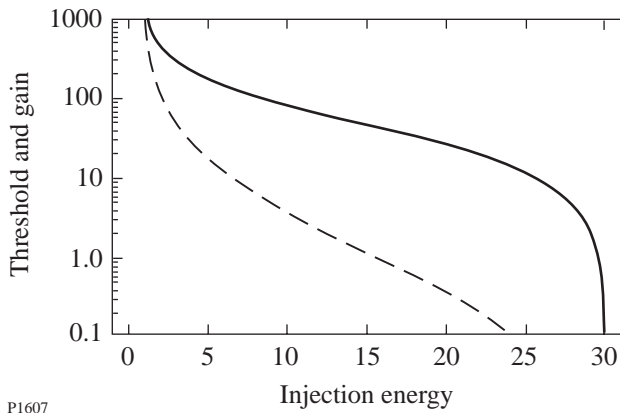
P1607

Figure 67.17
Threshold intensity a_B^2 required to repel the particle (broken line) and the corresponding gain in particle energy (solid line) plotted as functions of the particle injection energy for the case in which $\gamma_P = 30$. Energy is measured in units of the particle rest mass.

With a_B^2 fixed, the injection energy required to ensure that the particle is repelled by the pulse and the corresponding energy gain are functions of γ_P. By inverting Eq. (9), one finds that

$$\gamma_A = \gamma_P \mu_B - \left[(\gamma_P^2 - 1)(\mu_B^2 - 1) \right]^{1/2}, \qquad (11)$$

where $\mu_B = \left(1 + a_B^2/2 \right)^{1/2}$ is a measure of the pulse intensity. When $\gamma_P > \mu_B \gg 1$, Eq. (11) reduces to

$$\gamma_A \approx \frac{1}{2} \left(\frac{\gamma_P}{\mu_B} + \frac{\mu_B}{\gamma_P} \right) + \frac{1}{8} \left(\frac{\gamma_P}{\mu_B^3} + \frac{\mu_B}{\gamma_P^3} - \frac{2}{\gamma_P \mu_B} \right). \qquad (12)$$

When $\gamma_P \sim \mu_B$, the first and second terms of Eq. (11) are adequate, and, when $\gamma_P \gg \mu_B$, the first and third terms are adequate. In the latter limit Eq. (10) reduces to

$$\delta\gamma \approx 2\gamma_P \mu_B - \gamma_P/\mu_B. \qquad (13)$$

The injection energy and energy gain are plotted as functions of γ_P in Fig. 67.18 for the case in which $a_B^2 = 10$. The approximate formulas (12) and (13) are accurate and show clearly how the injection energy and the energy gain scale with γ_P and μ_B.

Subject to the constraints described between Eqs. (4) and (5), the preceding analysis is directly applicable to the accel-
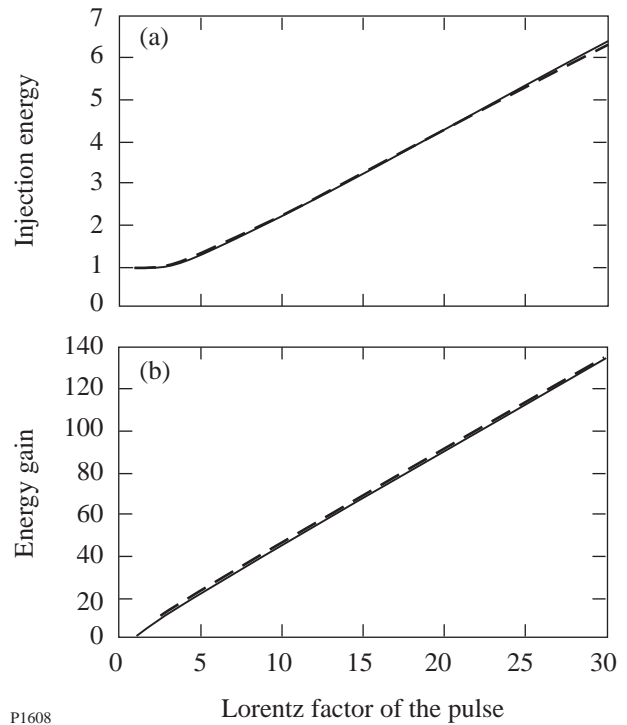
P1608

Figure 67.18
Injection energy required to ensure that the particle is repelled (a) and the corresponding gain in particle energy (b) plotted as functions of the Lorentz factor associated with the pulse for the case in which $a_B^2 = 10$. Energy is measured in units of the particle rest mass. The broken lines represent the approximate results [Eqs. (12) and (13)], whereas the solid lines represent the exact results [Eqs. (10) and (11)].

eration of a test electron in a plasma. However, one must also consider the motion of the background electrons under the influence of the pulse.

In the absence of collective effects, the background electrons behave like independent test particles. Provided that $a_B^2 < 2(\gamma_P^2 - 1)$, the background electrons pass freely through the pulse: although there is a temporary exchange of energy between the pulse and the background electrons (which is why the pulse speed is less than c), none of the pulse energy is lost to the plasma. It is for this reason that the test electron must be preaccelerated.

In the presence of collective effects, the compression of the electron fluid by the leading edge of the pulse produces a charge nonuniformity that, in turn, produces a longitudinal electric field. This longitudinal field modifies the motion of the electron fluid and the conclusions of the preceding paragraph. The electron-fluid momentum equation can be written in the form[10]

$$\partial_t \left(u_\parallel - a_\parallel \right) = -\partial_x \gamma , \qquad (14)$$

from which follows a conservation equation similar to Eq. (5). By using this conservation equation, one can show that the longitudinal potential evolves according to

$$\frac{d^2 a_\parallel}{dt^2} = \frac{1}{r^2 - 1} \left\{ r - \frac{r - a_\parallel}{\left[1 + \left(r - a_\parallel \right)^2 - r^2 - \left(r^2 - 1 \right) u_\perp^2 \right]^{1/2}} \right\} . \qquad (15)$$

In the low-intensity regime, Eq. (15) reduces to the equation for a driven linear oscillator, the behavior of which is well known: A short pulse provides an impulse to the plasma, which continues to oscillate after the pulse has passed. This oscillation, which is referred to as the wake of the pulse, can be removed by a second impulse that counteracts the first. In contrast, a long pulse produces an adiabatic plasma response. A pulse of infinite duration leaves no wake, whereas a pulse of finite duration leaves a wake, the amplitude of which depends on the ratio of the plasma period and the duration of the pulse. In the high-intensity regime the intrinsic plasma oscillation is nonlinear.[11] However, the plasma response is similar to that described above, as shown in Figs. 67.19 and 67.20. In Fig. 67.19(b) the first pulse loses energy to the second pulse at the same rate as the pulse loses energy to the wake in Fig. 67.19(a). Thus, a short pulse, which contains only a
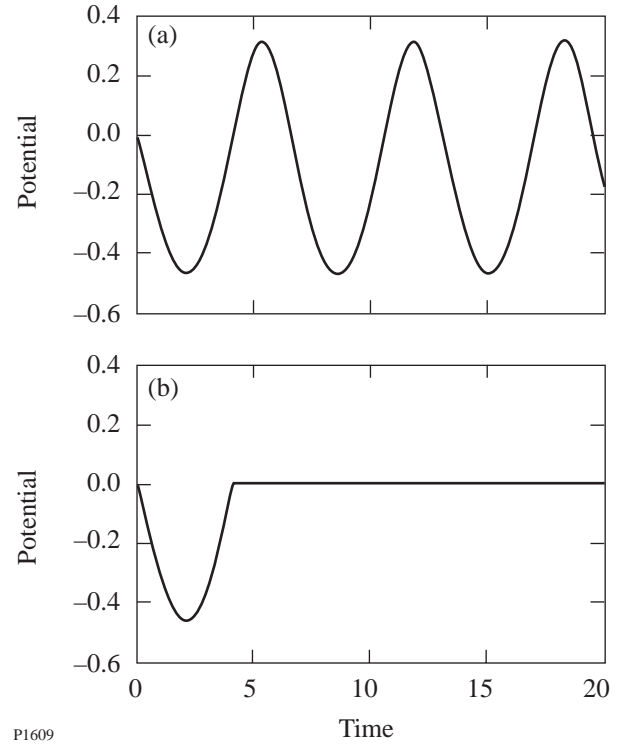

Figure 67.19

Longitudinal vector potential (wake) generated by a pulse of intensity $a^2 = 10\sin^2(t/t_P)H(t)H(t_P - t) + 10\sin^2\left[(t - t_D)/t_P \right]H(t_D)H(t_D + t_P - t)$ for the case in which $\gamma_P = 30$ and $t_P = 0.1$. Time is measured in units of the inverse of the electron plasma frequency: (a) $t_D = \infty$; (b) $t_D = 3.99$.

small amount of energy initially, is depleted quickly, whereas a long pulse, which contains a large amount of energy initially, is depleted slowly.

It is clear from Figs. 67.19 and 67.20 that a longitudinal field is generated within the pulse. The density nonuniformity associated with this longitudinal field modifies the transverse current and, hence, the pulse itself. Two-dimensional effects are also important. The pulse must be wide enough for the test electron to complete its transverse rotations without being deflected by the transverse ponderomotive force. This force also tends to expel background electrons from the neighborhood of the pulse.[5,12] If this expulsion is slow, the reduction in group speed of the pulse will be produced by the plasma through which most of the pulse will propagate. If the expulsion is rapid, most of the pulse will propagate in a plasma channel, or waveguide, and the reduction in group speed of the pulse will be produced by the waveguide. All of these effects must be included in a detailed study of this acceleration scheme.
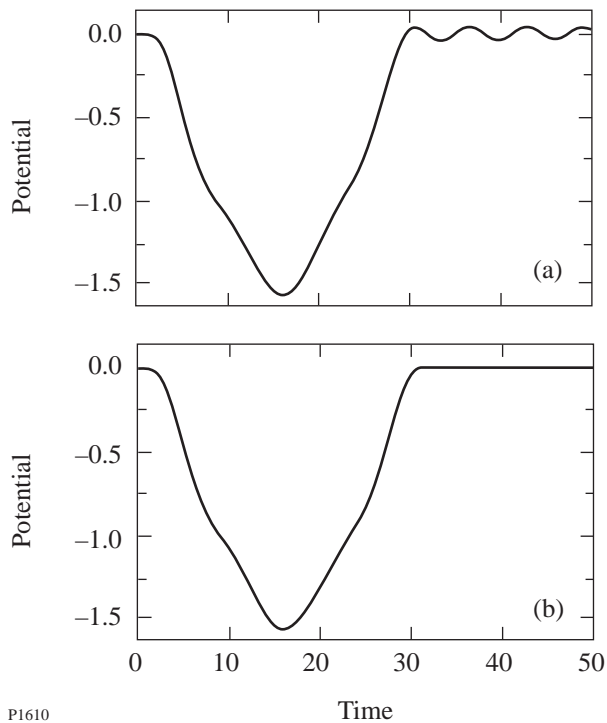
P1610

Figure 67.20

Longitudinal vector potential (wake) generated by a pulse of intensity $a^2 = 10\sin^2(t/t_P)H(t)H(t_P - t)$ for the case in which $\gamma_P = 30$. Time is measured in units of the inverse of the electron plasma frequency: (a) $t_P = 10.0$; (b) $t_P = 10.3$.

In summary, the motion of an electron in the electromagnetic field associated with a circularly polarized laser pulse in a plasma was studied. It appears possible to increase significantly the energy of a preaccelerated electron. While wake generation renders this acceleration scheme less than ideal, its simplicity is noteworthy. The wake fields produced by short laser pulses have been observed recently.[13,14] Future experiments will study the interaction of a preaccelerated bunch of electrons with such wake fields. One would only need to change the timing of the electron bunch in these experiments to test the scientific feasibility of this scheme.

REFERENCES

1. D. M. Wolkow, Z. Physik **94**, 250 (1935).

2. L. D. Landau and E. M. Lifshitz, *The Classical Theory of Fields*, 4th rev. ed. (Pergamon Press, Oxford, 1975), pp. 112 and 118.

3. M. D. Perry and G. Mourou, Science **264**, 917 (1994).

4. C. I. Moore, J. P. Knauer, and D. D. Meyerhofer, Phys. Rev. Lett. **74**, 2439 (1995).

5. P. Sprangle, E. Esarey, and J. Krall, Phys. Plasmas **3**, 2183 (1996).

6. H. Goldstein, *Classical Mechanics*, 2nd ed. (Addison-Wesley, Reading, MA, 1980), p. 303.

7. C. D. Decker and W. B. Mori, Phys. Rev. E **51**, 1364 (1995).

8. R. B. Palmer, in *Frontiers of Particle Beams*, edited by M. Month and S. Turner, Lecture Notes in Physics, Vol. 296 (Springer-Verlag, Berlin, 1988), p. 607.

9. M. Born and E. Wolf, eds. in *Principles of Optics*, 6th ed. (Pergamon Press, Oxford, 1980), p. 28.

10. C. J. McKinstrie and D. F. DuBois, Phys. Fluids **31**, 278 (1988).

11. V. I. Berezhiani and I. G. Murusidze, Phys. Lett. A **148**, 338 (1990).

12. H. M. Milchberg *et al.*, Phys. Plasmas **3**, 2149 (1996).

13. J. R. Marqès *et al.*, Phys. Rev. Lett. **76**, 3566 (1996).

14. C. W. Siders *et al.*, Phys. Rev. Lett. **76**, 3570 (1996).

A New Approach to the Analysis of the Thermal Equilibration of Optically Excited States

Mechanisms and rates of relaxation of optically excited states are important in the study of almost every material. They often determine the efficiency of some desired photoeffect and usually carry interesting information about the excited states themselves. Many fluorescent systems have been analyzed on the basis of the "universal relationship" introduced by Kennard and by Stepanov (K-S). These analyses frequently claim experimental confirmation of the applicability of the fundamental K-S assumption, namely, that the manifold of states associated with an excited electronic state have reached thermal equilibrium by the time of emission. The K-S prediction is that a certain function $F(v)$ will be linear in v with slope $-h/k_B T$, where T is the ambient temperature. A more precise look at the K-S function, reported here, reveals the possibility of extensive lack of excited-state thermal equilibration. The spectral K-S temperature $T^*(v) = -(h/k_B)/(dF/dv)$ is introduced, and it is found to be seldom close to T in a sampling of spectral data from various systems. While $T^*(v)$ does not necessarily represent an actual molecular temperature, its variation can be modeled in broadband systems by assuming coupled emitting and absorbing submanifolds that are demonstrably far from the equilibrium envisaged by Kennard and Stepanov.

Introduction

Kennard[1] was probably the first to predict the following general relation between the shapes of the absorption and fluorescence spectra of a homogeneous substance:

$$F(v) = \ln\left(\frac{c^2}{8\pi h}\frac{I(v)}{v^3\sigma(v)}\right) = -\frac{hv}{k_B T} + D(T).\qquad(1)$$

Here $I(v)$ is the emissive power (W·Hz^{-1}) at frequency v, $\sigma(v)$ the absorption cross section at that frequency, T the ambient temperature, and $D(T)$ a quantity independent of frequency. Stepanov[2] revived interest in the relation in 1957, and it has been widely attributed to him. Others have developed the concept and formulated it for organic molecules, photosyn-

thetic systems, semiconductors, and inhomogeneous systems.[3-7] Its application has generally focused on the goodness of the fit of experimental data to the linear function of frequency suggested by Eq. (1), and the translation of the results into a judgment of how well the excited state has attained thermal equilibrium before emission.

In Stepanov's version of the theory, relation (1) will hold if two conditions are satisfied: first, the aforementioned equilibrium, and second, that "non-exciting absorption" (due to transitions between two vibrational levels of the ground state) is negligible. The relation is frequently violated, and we shall see that these two assumptions alone do not give one a sufficiently broad basis to understand the violations.

Original Theory

Equation (1) is very general, but since it is known and applied largely by workers in biofluorescence, we review its derivation. It is a result of applying the Einstein A-B relation to sets of transitions (Fig. 67.21) in a system characterized by a metastable excited-state population. In the intensity, temperature, and wavelength regimes of interest, stimulated emission is entirely negligible. Thus[2,3]

$$\frac{I(v)}{\sigma(v)} = \frac{Z\int g'(w')A(w',v)p(w')dw'}{Z'\int g(w)B(w,v)\exp(w/k_B T)dw},\qquad(2)$$

where g and g' are the ground- and excited-state densities of states, respectively; Z and Z' are the partition functions for the ground and excited manifolds, respectively; and A and B are the Einstein coefficients. The important function $p(w')$ is proportional to the probability of occupation of the states at w' and will be central to our subsequent discussion. When the A-B relation is introduced with concern for densities of states,

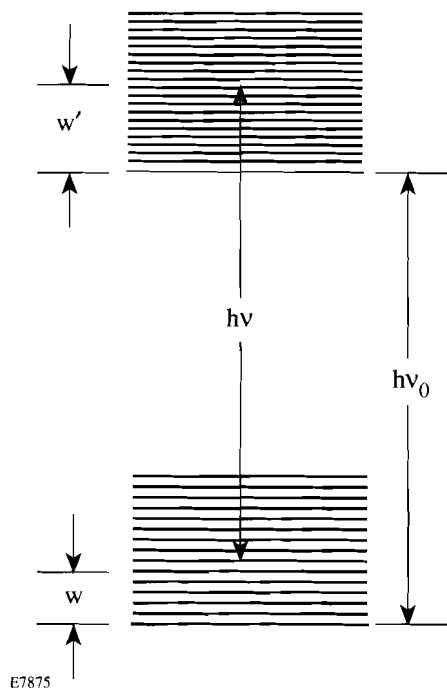$$g'(w')A(w',v)dw' = \frac{8\pi h v^3}{c^2}g(w)B(w,v)dw,\qquad(3)$$

Figure 67.21
Relative positions of the energy levels involved in constructing Eq. (5), showing a transition at energy hv between two different vibrational sublevels of the ground (w) and excited (w') states.

we obtain

$$\frac{c^2}{8\pi h}\frac{I(v)}{v^3\sigma(v)} = \frac{Z\int g(w)B(w,v)p(w')dw}{Z'\int g(w)B(w,v)\exp(-w/k_BT)dw}. \quad (4)$$

At each v, the states in the vicinity of w' are connected to specific groups of states in the vicinity of w in the lower manifold, and their energies are related by

$$hv_0 + w' = hv + w; \quad (5)$$

therefore,

$$\frac{c^2}{8\pi h}\frac{I(v)}{v^3\sigma(v)} = \frac{Z\int g(w)B(w,v)p(w+hv-hv_0)dw}{Z'\int g(w)B(w,v)\exp(-w/k_BT)dw}. \quad (6)$$

Equation (6) is still quite general, and, when p is replaced by the Boltzmann distribution and hv_0 is set equal to zero, it reduces to the Wien law at photon frequencies of interest to us. What distinguishes the fluorescent case from the blackbody case is that the fluorescence has an artificially induced meta-

stable population based on the energy hv_0 (such as, for example, the 0-0 electronic energy separation in a complex molecule). Kennard and Stepanov assumed such a metastable situation in a fluorescent system and made the further key assumption that the excited system was thermally equilibrated:

$$p(w') = \exp(-w'/k_BT) = \exp[-(w+hv-hv_0)/k_BT]. \quad (7)$$

Introduction of this distribution into Eq. (6) leads immediately to Eq. (1) and tells us that the quantity $D(T)$ is the system-specific quantity $hv_0/k_BT + \ln(Z/Z')$. The careful identification of $D(T)$ is due to Neporent.[3]

Ordinarily, the relation (1) is checked for a substance by finding the slope of $F(v)$ from experimental data and comparing T, as determined from this slope, with the ambient temperature. The most reliable data are those from the Stokes region, where both absorption and emission are at a high fraction of their maximum values. Experimenters have almost always found the relationship to be "half-right"—the function $F(v)$ is a reasonably straight line over much of the Stokes region, but, remarkably, the deduced value of T has seldom agreed with the ambient temperature. In Fig. 67.22, taken from

Figure 67.22
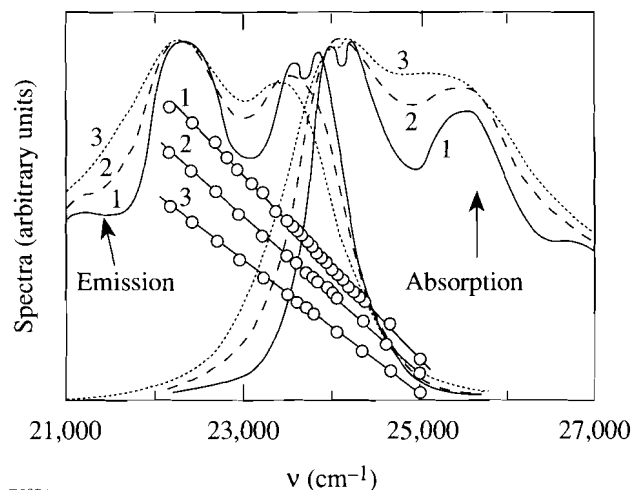Absorption and emission spectra of perylene vapor at (1) 513 K, (2) 633 K, and (3) 713 K, and the corresponding Kennard-Stepanov functions (straight lines). Note the correct qualitative temperature dependence of the slope of $F(v)$. These straight lines cover over three decades on the vertical scale and yield effective temperatures 556 K, 655 K, and 755 K, respectively. After Borisevich and Gruzinskii.[8]

Borisevich and Gruzynskii,[8] it is seen that the effective temperature T^* deduced from the slope is 20 K to 60 K higher than ambient. In some cases T^* has been as high as twice ambient temperature; in a few cases it has been lower. There has been much speculation as to the causes of these particular deviations from the relation. Many cases are reviewed and discussed by Van Metter and Knox,[6] who evaluated inhomogeneous broadening as a possible cause.

Alternative Approach

The observed linear function that remarkably arises from very complex input is a broad confirmation of the "universal relation," but its failure in detail is symptomatic of the possibility of a very complex nonequilibrium distribution during the lifetime of the fluorescence. The experiments yielding $T^* \neq T$ seem to tell us that this distribution is nearly equilibrated, although the conclusion that the excited molecule has a "warm" environment is inconsistent with a single temperature appearing in the theory.[6] Here we report a new method of analyzing the Kennard-Stepanov data that highlights the deviation from a Boltzmann distribution. We find that the failure of the slope to produce an ambient temperature value is only one aspect of this deviation, and we set forth a phenomenological theory on the basis of which some of the observations can be understood.

We define the Kennard-Stepanov spectral temperature in terms of the local slope of $F(v)$:

$$T^*(v) \equiv -\left[\frac{k_B}{h} \frac{dF(v)}{dv}\right]^{-1}$$

$$= -\left\{\frac{k_B}{h} \frac{d}{dv} \ln\left[\frac{c^2}{8\pi h} \frac{I(v)}{v^3 \sigma(v)}\right]\right\}^{-1}. \tag{8}$$

This device transforms the rather prosaic experimental $F(v)$ into a spectrum which, in most cases seen to date, is rich in detail. There are peaks, valleys, plateaus, and sometimes divergences. In virtually no case to date have we found a constant $T^*(v)$, as the K-S relation predicts. $T^*(v)$ curves computed from data sets in several typical cases[9–12] are shown in Fig. 67.23. A frequently seen feature is that $T^*(v)$ remains fairly constant either near ambient temperature or somewhat above it over much of the frequency range but includes one or more peaks.

In practice, $T^*(v)$ is found from the inverse slope of the regression line through $F(v)$ for a series of data points centered at frequency v. The width of the derivative window can be
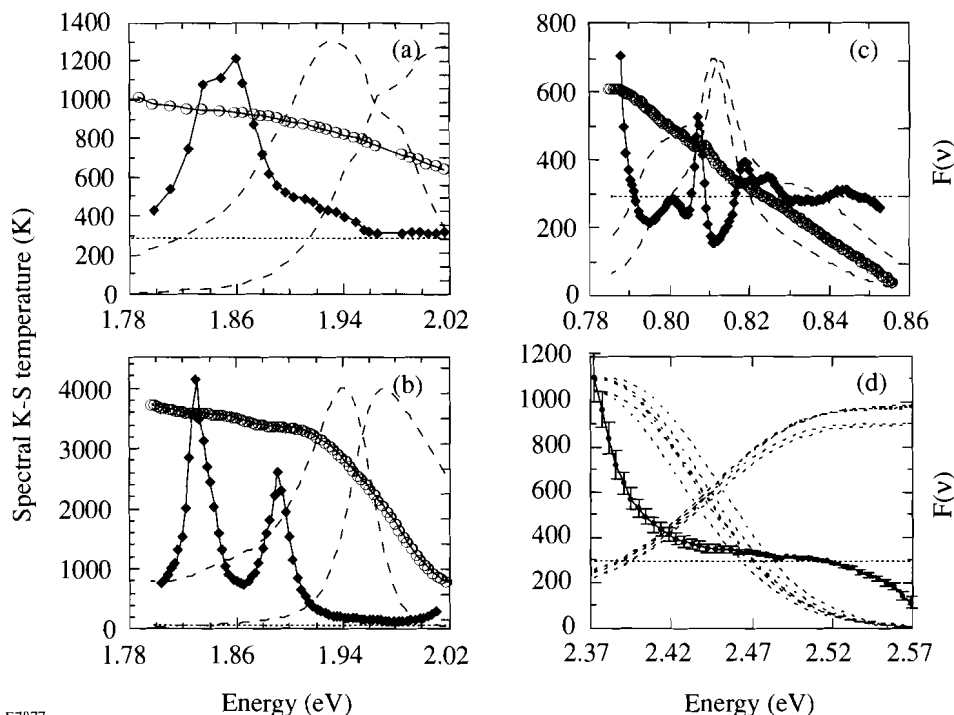
Figure 67.23
Experimental $T^*(v)$ spectra (filled diamonds) and the parent $F(v)$ (open circles). Dashed curves in the background are emission (on the left) and absorption (on the right). Spectra are in arbitrary units, $T^*(v)$ is in K, and the variation of $F(v)$ is indicated by tick marks, separated by factors of 2.303, at the right of each frame except (d). The abscissa is frequency in energy units. (a) α–phycocyanin, 295 K (K. Sauer[9]); (b) α–phycocyanin, 77 K (M. Debreczeny et al.[10]); (c) erbium-doped silicate glass, 295 K (R. Giles and DeSurvire[11]); (d) poly(p-phenylene vinylene), PPV.[12] In each case the constant value of the ambient temperature, which is the prediction of the universal relation for T^*, is shown as a horizontal dotted line. In (d), the spectral temperature computed from six absorption-emission pairs is shown as a mean with standard deviation indicated by error bars.

E7877

varied. A larger window is necessary when there seems to be a great deal of experimental noise. In most cases, the slope has been best found over a number of data points ranging between 5 and 11. Generally, changing the width of the derivative window has only a very slight effect upon the contour of $T^*(v)$. By introducing artificial noise and artificial miscalibrations into simulated data, we have satisfied ourselves that the structures seen are not artifacts of the method. Also, the effects appear to be reproducible, as will be discussed.

Before discussing the possible origins of the structure appearing in Fig. 67.23, we describe the materials on which it is based. We have found it difficult to rely on the published literature for the accuracy necessary in this study, so in most cases unpublished data in electronic form have been used. Figures 67.23(a) and 67.23(b) refer to solutions of a subunit of an important photosynthetic antenna protein, α-phycocyanin (α-PC). Figure 67.23(a) shows one of the first cases we analyzed. Kenneth Sauer,[9] who brought its unusual K-S behavior to our attention several years ago, computed $F(v)$ from room-temperature fluorescence and absorption spectra of α-PC representative of samples from four different organisms (Switalski[13]). The four α-PC had similar fluorescence, absorption, and circular dichroism spectra, similar time-resolved fluorescence behavior, and high fluorescence polarization across the entire band of excitation wavelengths. Care was taken to test for the presence of α-β heterodimers.

The data from which Fig. 67.23(b) was produced were those of Debreczeny and colleagues.[10] Again the system is the subunit α-PC, this time at 77 K in a buffer of 5 mM phosphate at pH 7.0 with 75% glycerol by volume. The small rise near 2.02 eV should be ignored as it may be a result of scattering from the 560-nm excitation source.

Figures 67.23(c) and 67.23(d) show K-S analyses for two materials of interest to applied physics. The former represents room-temperature Er-doped silicate glass co-doped with Al and Ge,[11] one of the important materials for use in fiber light amplifiers. The latter shows spectral temperatures computed from the spectra of a series of poly(p-phenylene vinylene) (PPV) samples,[12] materials of interest for use in light-emitting diodes. The several cases shown represent data from samples subjected to different periods of aging. The case of Fig. 67.23(c) illustrates the remarkable amount of structure that sometimes presents itself in terms of a K-S spectral temperature. Figure 67.23(d) will be discussed later as an example of reproducibility of the curves.

Model Calculations

The existence of peaks in certain $T^*(v)$ data may be understood physically on the basis of the following straightforward model. A system of fluorescing states is considered as a mixture of individual systems within each of which there is thermal equilibration and among which detailed-balance kinetics with adjustable rates can be applied. This is a natural development of an idea introduced by Band and Heller.[7] In terms more closely related to our context, each subsystem of fluorescers is a "K-S system" that contributes absorption and fluorescence components obeying Eq. (1) but whose populations relative to each other are kinetics-dependent. The subsystems may in fact be chemically different molecules or sets of chemically identical molecules that are inhomogeneously broadened, or they may represent manifolds associated with different electronic states of each molecule of a homogeneous species.

It is readily shown that the K-S function for the K-S mixture just described is given by

$$F(v) = \ln\left\{\sum_i \bar{p}_i \xi_i(v) \exp\left[F_i(v)\right]\right\}, \qquad (9a)$$

where $\bar{p}_i$ is the average relative population of the emitting subset i, $F_i(v)$ is the K-S function for that subset, and

$$\xi_i(v) = \frac{\sigma_i(v)}{\sum_j \sigma_j(v)}. \qquad (9b)$$

From this, we can discern that, for a system in which the absorption and emission spectra are linear combinations of the individual spectra of n species, each of which obey Eq. (1), $F(v)$ will have n asymptotes of slope $-h/k_B T$. In a mixture of two species that do not exchange excitation energy (noninteracting species), the spacing between the intercepts will be equal to the difference between the two values of $D(T)$. The two asymptotes of $F(v)$ can be seen clearly in Fig. 67.24(a), which depicts the partially resolved absorption and fluorescence spectra along with $F(v)$ and $T^*(v)$ associated with two manifolds that are not exchanging excitation energy. These manifolds are represented by Gaussian absorption peaks centered at 1.810 and 1.851 eV, each with 17-meV FWHM. Since the manifolds correspond to "good K-S systems," the two emission bands are automatically determined.
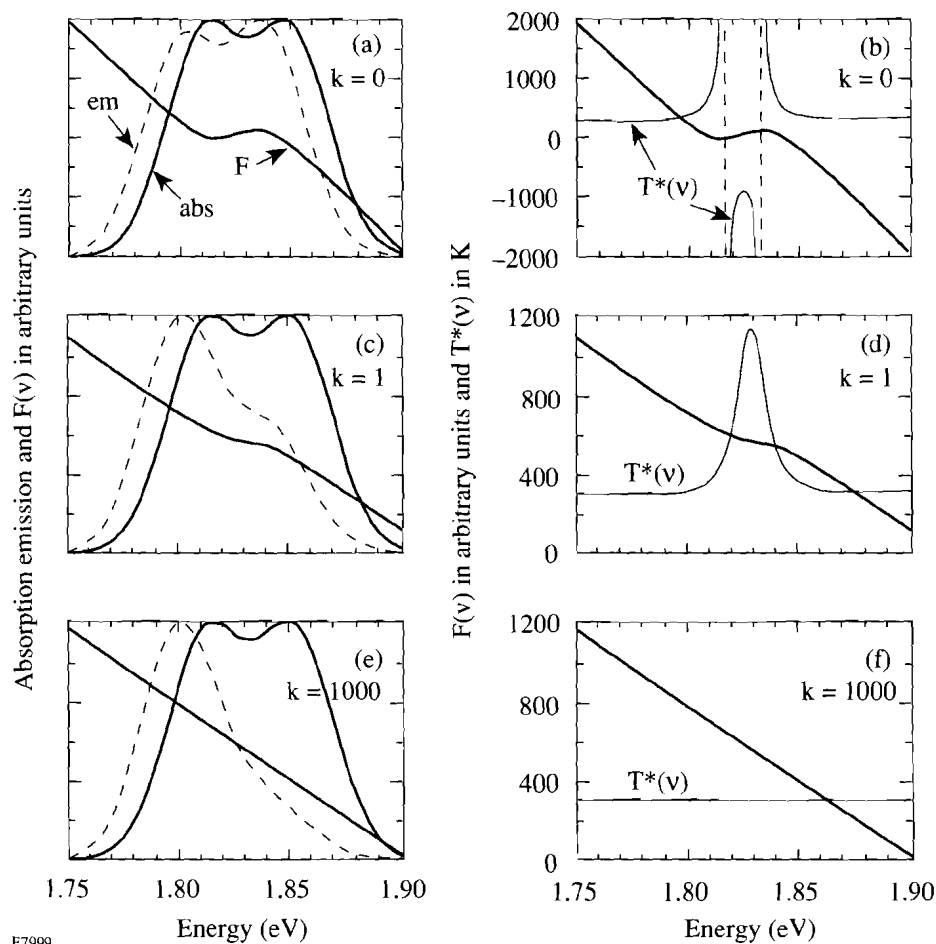
E7999

Figure 67.24
Results of a model calculation of $F(v)$ and $T^*(v)$ for two manifolds interchanging populations with rate constants k, downward, and $k\exp(-\Delta/k_B T)$, upward. $F(v)$ curves, heavy line, are shown in all parts of the figure; the spectra from which they derive are shown in (a), (c), and (e), and $T^*(v)$ is shown as indicated in (b), (d), and (f). The total dipole strength is the same in each spectral manifold and is distributed as two resolved Gaussian absorption and emission bands. The absorption FWHM of the individual bands, whose centers are located at 1.810 and 1.851 eV, is 17 meV. The total absorption and emission are shown as thin solid and dashed lines, respectively, adjusted to full scale. The lifetime of each manifold is taken to be 1.0 ns and k is expressed in units of $(1.0 \text{ ns})^{-1}$. Broadband excitation is assumed. As k increases, top to bottom, the kink in the $F(v)$ curve flattens out and $T^*(v)$ progresses from divergent (b), to peaked (d), to constant (f).

Exchange of excitation between the manifolds makes the situation slightly more complex. We solve the kinetic equations for the steady-state manifold populations $\bar{p}_i$, assuming that the exciting light is constant and using transfer rates, intrinsic quantum yields, relative oscillator strengths, and spectral shape functions as inputs. We assume a rate k for transfer from the upper to the lower manifold and, in keeping with detailed balance, a rate $k\exp(-\Delta E/k_B T)$ from lower to upper. For our particular spectra, $\exp(-\Delta E/k_B T) = 0.145$ at $T = 300$ K. In each manifold we take $Z = Z'$ and unit quantum yield for simplicity. Figures 67.24(c) and 67.24(e) illustrate the effect of increasing k; the curvature in $F(v)$ is completely smoothed out as k reaches 1000 times the fluorescence rate. Correspondingly, as one may see by scanning Figs. 67.24(b), 67.24(d), and 67.24(f) from top to bottom, there is a dramatic effect on $T^*(v)$ as the excited state approaches an equilibrium condition. At the same time, one sees the emission shifting from an equal mixture of both bands [Fig. 67.24(a)] to predominant emission from the lower band [Figs. 67.24(c)

and 67.24(e)]. A peak in $T^*(v)$ appears at relatively small excitation exchange rate, which is a significant result. To the extent that such modeling is appropriate, it appears to indicate that the various systems involved in Fig. 67.24 exhibit considerable nonequilibration preceding fluorescence. A more extensive range of parameters has been studied[14] and further work is planned.

More generally, there will be at most $n-1$ peaks in $T^*(v)$ for n excited manifolds. These peaks correspond to the visibly nonlinear portions between the asymptotes of $F(v)$. When $F(v)$ includes one or more segments of positive slope, $T^*(v)$ will be undefined where the slope momentarily crosses zero, and may become negative, as in Fig. 67.24(b). The number of species present is not necessarily evident from looking at a plot of $T^*(v)$ because some of the peaks may be small enough to be indistinguishable from experimental noise or two or more peaks may be so close together that they resemble one.

Discussion

The full modeling of spectra must account also for $T^*(v)$ dropping below ambient, in some cases becoming divergent. Our exploration of parameter space has shown that dips below ambient are indicative of the higher-energy species having a low quantum yield, and that divergences occur when there is broadband excitation of weakly coupled manifolds whose separation is greater than their widths. Variation in the curves with excitation wavelength is readily treated with the kinetic model, in analogy with the variation of the standard T^*, discussed and reviewed by Van Metter and Knox.[6] Variation of the standard T^* was observed in splendid detail recently by Sechkarev and Beger[15] in adsorbed rhodamine 6G, a system for which the present method should provide an even richer basis for analysis of the relaxation.

The systems of Fig. 67.23 are complex, and we have had only limited success in fitting the curves using this elementary relaxation model. The α-PC peaks in Figs. 67.23(a) and 67.23(b) are sufficiently stable and reproducible that the existence of poorly coupled states, as in our model, is a good possibility. Should they represent impurities, it is clear that the K-S analysis is a sensitive method for locating them. The T^* variations of Figs. 67.23(c) and 67.23(d) may well be indicative of single-manifold K-S failure. Another consideration is inhomogeneous broadening,[6] which, in a case involving a single species, causes an upward shift in the value of the ordinary T^* and, if the excitation is not broadband, introduces some weak v dependence into $T^*(v)$. Adding inhomogeneous broadening into the computer simulation might make it possible to model a case resembling the 77 K data of Debreczeny et al.[10] [Fig. 67.23(b)], in which the contour of the $T^*(v)$ plot resembles the theoretical case of a mixture of species, but in which $T^*(v)$ never goes as low as the ambient temperature.

It is necessary to address the question of reproducibility of the experimental effects. Of course, this is primarily a matter of reproducibility of the spectra involved, but $T^*(v)$ senses small relative changes, in analogy with derivative spectroscopy. In the case of α-phycocyanin, Debreczeny's 295 K data (not shown) is very similar to Sauer's [Fig. 67.23(a)], a main peak occurring at 1.87 eV and an additional one outside Sauer's range at 1.80 eV. As the temperature is lowered, these peaks apparently shift and interchange strengths, ending up at 1.89 and 1.83 eV at 77 K [Fig. 67.23(b)]. The data on PPV [Fig. 67.23(d)] provide a good example of $T^*(v)$ reproduc-

ibility. The several dashed curves shown are absorption and emission spectra of six different samples. While in this case the data come from the same laboratory,[12] each sample was grown from a different precursor aged for six separate periods of time. When judging reproducibility, we must recognize that the utility of the $T^*(v)$ analysis brings with it the cost of high sensitivity to those experimental conditions that affect equilibrium among various manifolds of states.

Conclusions

We have shown the usefulness of plotting a new function $T^*(v)$ in order to magnify regions of nonlinearity in the K-S function that analyzes equilibration in fluorescing excited states. The nonlinearity of these plots has long been smoothed over in their interpretation. As we have seen, however, peaks in $T^*(v)$ could be sensitive indicators of the presence of hidden excited states or impurities with which there is incomplete thermal equilibration. $T^*(v)$ should prove useful as a means of estimating transfer rates in complex molecules. We are persuaded by the data and by several preliminary theoretical results that our interpretation is correct, and that efforts to examine the full parameter space will be rewarded.

REFERENCES

1. E. H. Kennard, Phys. Rev. **11**, 29 (1918); Phys. Rev. **28**, 672 (1926).

2. B. I. Stepanov, Sov. Phys. Dokl. **2**, 81 (1957).

3. B. S. Neporent, Sov. Phys. Dokl. **3**, 337 (1958).

4. R. T. Ross, Photochem. Photobiol. **21**, 401 (1975).

5. D. E. McCumber, Phys. Rev. **136**, A954 (1964).

6. R. L. Van Metter and R. S. Knox, Chem. Phys. **12**, 333 (1976).

7. Y. B. Band and D. F. Heller, Phys. Rev. A **38**, 1885 (1988).

8. N. A. Borisevich and V. V. Gruzinskii, Opt. Spectrosc. **14**, 20 (1963).

9. K. Sauer, unpublished data (1987).

10. M. P. Debreczeny *et al.*, J. Phys. Chem. **97**, 9852 (1993); J. Phys. Chem. **99**, 8412 (1995).

11. C. R. Giles and E. Desurvire, J. Lightwave Technol. **9**, 271 (1991).

12. M. R. Robinson *et al.*, Polym. Mater. Sci. Eng. **74**, 292 (1996).

13. S. C. Switalski and K. Sauer, Photochem. Photobiol. **40**, 423 (1984); S. C. Switalski, Ph. D. thesis, University of California, Berkeley, 1986.

14. D. A. Sawicki and R. S. Knox, Phys. Rev. A (in press).

15. A. V. Sechkarev and V. N. Beger, Opt. Spectrosc. **72**, 303 (1992).

Overview of the Design and Implementation of the OMEGA Laser Control System Software

Over the last four to five years, the Laboratory for Laser Energetics has been in the midst of an Upgrade Project, which has resulted in the new OMEGA inertial confinement fusion (ICF) laser system. The previous OMEGA consisted of a 24-beam laser with its associated controls and diagnostics. Many of the components of the previous system were manually adjusted, and the control system consisted of several Digital Equipment Corporation VAX and PDP-11 computers and a custom-designed power conditioning computer system. Several IBM/PC–based diagnostics were also a part of this system. Much of the original control software had been written in the Forth language, but over the years it was largely rewritten in Fortran and C, making extensive use of DEC-specific libraries and language extensions.

In addition to upgrading the hardware for the new 60-beam laser, all of the laser controls were also redesigned. This redesign was necessary for a variety of reasons, the most compelling of which was the motorization of virtually every movable optic and component in the system. Other factors included the desire for more modern user interfaces and more platform-independent software systems (to take advan-

tage of the inevitable evolution in computer hardware and operating environments). The success in achieving these goals will be reviewed in a later section. First, an overview of the current design and some implementation details will be presented.

Laser Control System Overview

As shown in Fig. 67.25, which also appears in Ref. 1, p. 34, the top-down design of the newly upgraded OMEGA laser control system consists of an interconnected network of software executives. This control system has been developed using state-of-the-art techniques and tools, included C/C++, X-based Graphical User Interfaces (GUI's), Inter-Process Communication (IPC), and Lightweight Processes (LWP's or threads).

1. Choice of Platform

In choosing the primary computer platform, the factors that were considered included hardware and software price, speed, packaging, support and availability of operating systems, programming languages, and configuration management tools.
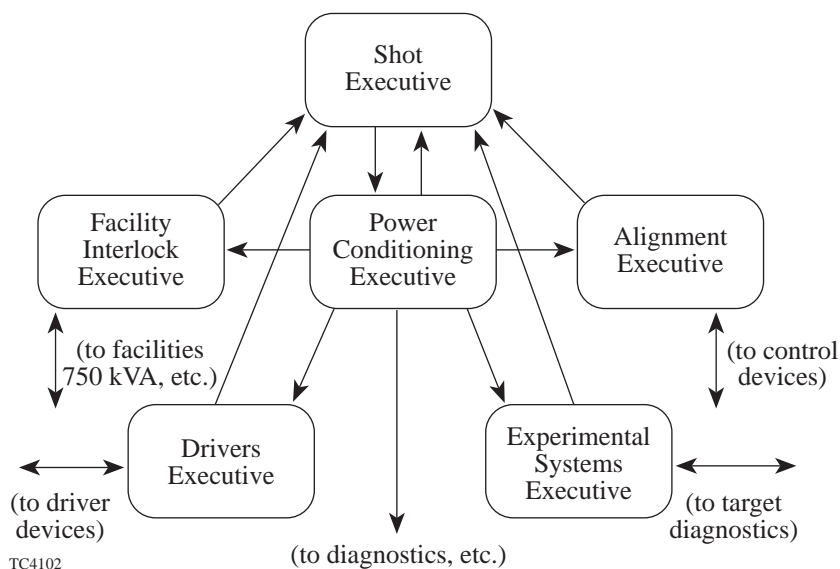

Figure 67.25
The laser control system is distributed over several *Executives* that are interconnected via Ethernet using TCP/IP. Each Executive performs or oversees one aspect of the laser operation and interacts with its associated devices.

TC4102

a. Computer hardware. The choice of platform for the primary control computers was a difficult one, and several of the recently developed *Reduced Instruction Set Computers (RISC)* were considered before the Sun Microsystems' SPARC architecture was selected. Other platforms that were considered included the DEC Alpha, IBM RS-6000, and HP 735. As mentioned, the primary factors used in selecting the computer hardware were price, speed, packaging, and support. Another consideration was the installed base at LLE and availability of experienced support people within the Laboratory. In the end, since there was no clear winner in the technical areas, this latter consideration may have been the deciding factor since LLE already had a large, installed base of Sun Microsystems' equipment and several years of experience with the administration of Sun systems.

b. Operating system. The operating system was a key factor in the choice of platform for this project (see previous paragraph). During the design phase of the control system it was decided that available standards would be followed wherever possible to ensure the longevity of the control system. For operating systems, it was decided that conformance to the ANSI/ISO/IEEE POSIX (**P**ortable **O**perating **S**ystem **I**nterface for Uni**X**) standard would be the selection criterion. Although the POSIX standard is designed to be generally applicable, this virtually implied that a UNIX operating system would be used. Although all of the platforms considered had available operating systems that claimed some level of POSIX conformance, some platforms were dropped from consideration because of an apparent limited support for their POSIX-conforming operating environments. The OMEGA executive-level computers are currently running Sun's Solaris 2.5 operating system, which complies with the POSIX.1[2] and POSIX.2[3] standards for operating system interfaces.

c. Programming languages. The primary languages used for this project were ANSI standard C[4] and C++,[5] based on standardization and performance. It was also decided that ANSI Fortran could be used where applicable. As the project has evolved, portions of the system have also been implemented using the PV-WAVE[6] system.

d. Threads. *Threads,* also known as *lightweight processes*, were identified in the design phase of the system as an important and valuable tool for implementing the control system. These threads are tightly coupled but asynchronously executing processes within a single program and are implemented in the OMEGA control system using Sun's multithreaded Solaris operating system API.

e. Graphical User Interfaces builders. As will be seen later, a key element of the OMEGA control system is the design of the various Graphical User Interfaces (GUI's). Two GUI builders[7] were employed in the development of the OMEGA control system: the UIM/X system from Visual Edge Software and the Data Views from V. I. Corporation. Each has advantages and disadvantages that make them both valuable. These GUI builders generate code for X/Motif GUI's, which is in turn linked with the application software through locally developed libraries and so-called "call-backs."

f. Configuration management tools. As mentioned, the new OMEGA control system is intended to be easier to maintain and more durable than the previous system. A key factor in the longevity of any system, including software systems, is configuration management. The OMEGA system employs the well-established UNIX/POSIX configuration management tool called **make,** and all revisions to source code are maintained by SCCS (Source Code Control System).

g. Auxiliary computer systems. A number of auxiliary systems on OMEGA are not operating on the Primary computer platform. The vast majority of these are IBM/PC-compatible systems, which are used generally for reasons of convenience or hardware interface availability. Wherever possible, the same languages and tools were used for developing software on these auxiliary systems, several of which will be mentioned in later sections.

The Executives

The upper-level control software for OMEGA is divided into several major programs, which are called *executives,* as shown in Fig. 67.25. These executives vary in complexity and function; however, they all share a number of features and make use of a number of the same subprocesses to perform their various tasks. Each executive follows, in some way, the vertical layout illustrated in Fig. 67.26. For the laser system to operate, several, if not all, of these executives must be operating and communicating with their associated devices and with each other. The next few sections will describe the design of several of the executives currently in use or being implemented; later sections will discuss the interface and support systems that are common across the executives.

1. Shot Executive

Although it was not available during the activation of the laser system, a key element in the ultimate operation of the laser system is the Shot Executive, also known as the Shot Supervisor. This executive is under the direct control of the
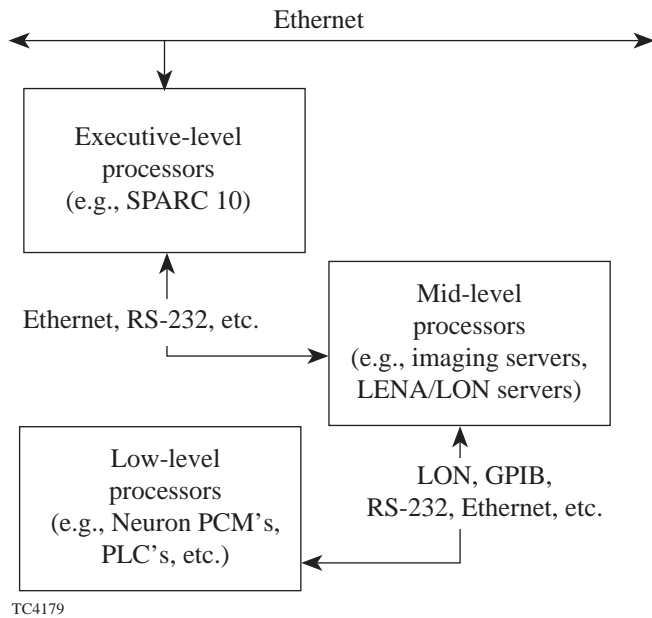
TC4179

Figure 67.26
The laser control subsystems are distributed vertically into executive, mid-level, and low-level processors. This organization facilitates both modular code development and reusability.

Shot Director, who is the single individual responsible for the operation of the laser.

This executive serves several purposes. In its current form, it acts primarily as a sort of *clearing house* for status information from various other executives and processes. It monitors the state of the laser system and determines whether the various subsystems are ready to proceed to a new state, as requested by the Power Conditioning Executive (PCE). This allows the Shot Director to monitor the system and, in the event of some problem, make the decision whether or not to proceed into the next state. This process of moving from state to state will be discussed in more detail in a later section and was discussed in much greater detail in Ref. 1, pp. 34–43.

This executive makes use of a library of C++ classes and functions that implement a state engine and messaging system. This library was generalized from code developed for the Power Conditioning Executive, which was discussed in detail in Ref. 1 and is also used by the Experimental Executive (discussed later in this article).

In addition, the Shot Executive uses the *Broadcast* system (described in Ref. 1, p. 38) to communicate with the other

executives. A standardized Graphical User Interface (GUI) allows the Shot Director to abort the *shot sequence* and to intervene should any other executive indicate that it is not prepared for a requested system state transition (see subheading Standard Graphical User Interface later in this article).

2. Facility Interlock Executive

The Facility Interlock Executive (FIE) was the first executive to be operational in the OMEGA control room. It provides a user interface to access all doors, shutters, personnel monitors, signs, beacons, sirens, and power cutoffs that constitute the safety-related subsystems of the OMEGA laser. In addition, the FIE communicates via the *Broadcast* system to the Power Conditioning Executive to inform it of the state of the 750-KVA power that operates the OMEGA power conditioning subsystem.

The FIE is implemented in two parts: The executive part is a standard GUI, which acts as both operator interface and status display. This part communicates over Ethernet using a low-level protocol to a Programmable Logic Controller (PLC), located in the main laser relay panel. This PLC has the safety-related logic programmed into it to ensure safe operation of the facility, even if the PLC should lose contact with the executive process. The PLC subsystems of OMEGA are discussed in more detail later.

Because of conflicts with the API (Application Programmers Interface) for the PLC, the FIE could not be implemented with the *threads* that were used in most of the other executives. This resulted in a number of changes in its design and increased the difficulty of its implementation.

3. Power Conditioning Subsystem

The design and implementation of the power conditioning subsystem has been described in detail in Ref. 1, pp. 34–42.

4. Alignment Executive

One of the most critical subsystems for activation and continued operation of the laser system is the Alignment Executive (AE). This executive provides access for the alignment operators to the several thousand controllable devices throughout the laser system. These devices are controlled individually or in groups by specially designed Neuron™[8] control modules, including the Two-State Control Module (TSCM), Single-Axis Control Module (SACM), and Dual-Axis Control Module (DACM). These devices are accessed via the LENA interface (see Ref. 1, pp. 38–39).

The AE itself has gone through several evolutionary stages, from an early form based on the Drivers Executive (see next paragraph), to its current, highly graphical interface. In its current form, the GUI, which was developed using the DataViews GUI builder, has interactive graphical representations of the various control devices, which allow both control and status displays. Additional pull-down menus allow more detailed control, as well as execution of macro scripts and saving and restoring of device locations.

5. Drivers Executive

Although recently largely rewritten for use in the Control Room, the Drivers Executive was the first executive made operational on the OMEGA system. In many ways, the Drivers Executive contains all of the features of the entire laser control system: device control, energy diagnostics, access to imaging, and GUI's. This made its implementation and deployment in the early stages of the OMEGA Upgrade extremely difficult. To make the job easier, the task was divided between several developers, and the executive divided into several semi-autonomous subprocesses (illustrated in Fig. 67.27).

While many aspects of this early executive have been eliminated or redesigned, the process of developing it was key to the evolution of the current design. In the current design, for example, the *process interface* has evolved into the current, much simpler *Broadcast* system or been replaced by direct interfaces.

Most of the diagnostic subprocesses of the Drivers Executive are still in place, including the imaging subsystem (see next paragraph plus later subsection on imaging).

6. Laser Diagnostics

Laser Diagnostics is not a separate executive *per se* but is a complex set of processes run in cooperation with the executives to obtain diagnostic information about several aspects of the laser system.

Associated with the Drivers Executive is a sophisticated suite of acquisition processes that interact with CAMAC-based diagnostics and oscilloscopes via several GPIB (General Purpose Interface Bus) interfaces.

Other key diagnostic interfaces are those for the calorimeters, which are Neuron™-based devices, and the harmonic energy diagnostic (HED) (see later subsection on imaging).

7. Experimental Systems Executive

The Experimental Systems Executive (ESE) is currently still in the design phase. In its first form, it will be similar in
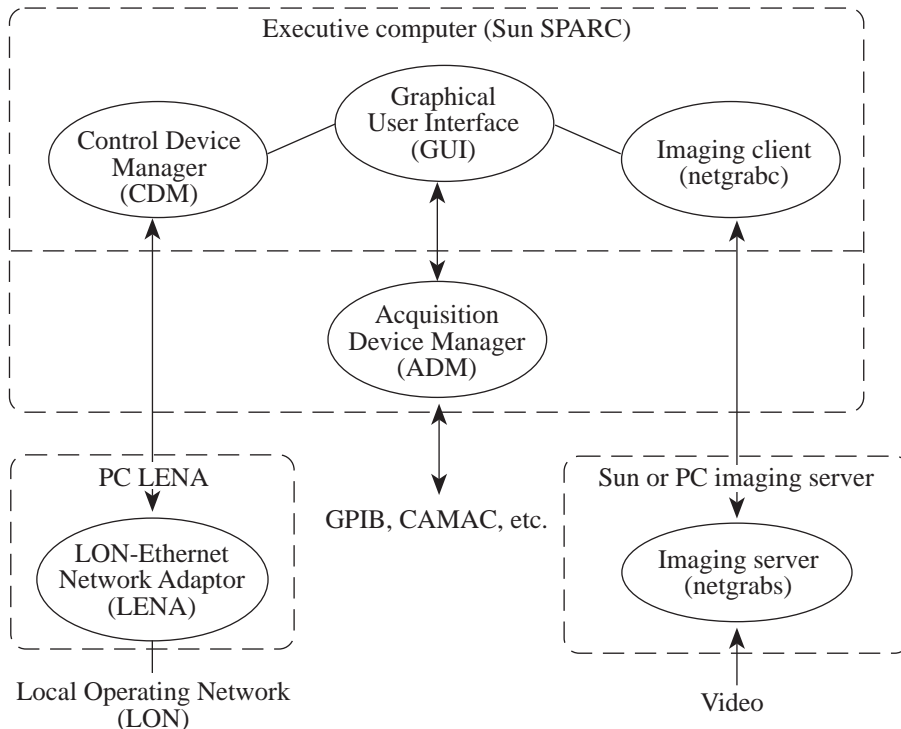

Figure 67.27
The original Drivers Executive included several important design features, i.e., distributed processing and a Graphical User Interface (GUI).

function to the Shot Executive (SE). It will coordinate the status information from the numerous experimental diagnostic subsystems and interact with the SE to allow the shot sequence to proceed.

a. TVS/TPS—Target Viewing and Positioning System. One subsystem of the ESE has been in operation for some time—the target viewing and positioning subsystem. This GUI provides access to the imaging system used for target viewing, and to the PLC used for control of the TVS controls and target positioner.

Interface/Support Systems

1. Imaging

The first operational system within the Alignment Executive on the upgraded OMEGA laser was the electronic imaging subsystem, which is used for alignment. This system includes nearly 100 cameras, video multiplexors, frame grabbers, and a cable TV–style video distribution system.

The control software for the imaging subsystem is divided into several layers, as illustrated in Fig. 67.28. Although a number of different GUI's have been and are being used, the same basic *netgrabc/netgrabs* subsystem is used in several OMEGA subsystems including the Alignment Sensor Packages (ASP's), Harmonic Energy Diagnostics (HED's), Target Viewing System (TVS), and Imaging X-Ray Streak Camera (IXSC).

In addition to being able to select, view, save, and restore images from the numerous cameras throughout the laser sys-

tem, the imaging system incorporates an extensive suite of image-processing routines that provide the alignment operators with immediate feedback on the positioning of the laser beams. This includes overlay of reference locations from the database (see 2. Database Interface) and computation of centers using various algorithms.

a. Alignment Imaging Graphical User Interface. A specialized and highly sophisticated GUI was developed to operate of the alignment imaging subsystem. This interface continues to operate in conjunction with the Alignment Executive.

2. Database Interface

The executives are interfaced to an Ingres database, which stores the laser and experimental data and maintains the various shot counters, including the *Database Log Number (DBL#)* that is incremented for all shots or aborts, and counters for the different shot types. As an example of the database's function, a precise record of the number of shots on each of the system's many thousand flash lamps is maintained. These records allow periodic maintenance to be performed in a timely manner. The post-shot data logged to the database can be used to review the amplifier performance on any shot or to perform statistical analysis of amplifier performance over time. In addition, post-shot reports are generated from the database, using this information as well as other diagnostic data that are stored in the database after the shot.

An earlier version of the executive software used a separate process called the *Data Manager* to communicate with the database. This was done because of an incompatibility be-
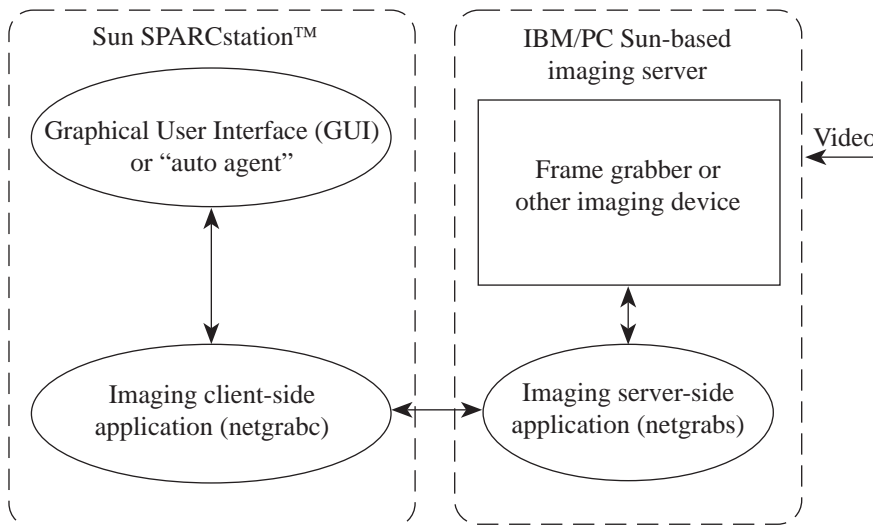

Figure 67.28
The imaging system design is general purpose and based on a network imaging server. This server is accessed over Ethernet via TCP/IP using Remote Procedure Calls (RPC's), and employs a Graphical User Interface (GUI).

TC4178

tween the multithreaded executives and the database API. Recent updates to the database system have allowed this functionality to be merged directly into the executives, resulting in a significant improvement in performance as well as simplicity and reliability. The database API has been written in ANSI C for compatibility with a variety of applications.

a. Image/data archive. One lesson learned on the previous OMEGA laser system was that there is a need for a coordinated system to deal with experimental data, including images from film and electronic detectors, as well as trace and point data from various detectors.

The approach taken on the new OMEGA system is to provide an interface through the Ingres database to a separate archive of this data. Currently, there is an experimental interface to this archive making use of a World Wide Web interface system (e.g., Netscape) to allow access to the data from any of the various computer systems within the Laboratory. The design of the image/data archive is illustrated in Fig. 67.29.

3. Standardized Graphical User Interface

Most of the executives have been designed with a standardized Graphical User Interface (GUI), both to maintain a uniform and aesthetic appearance and to aid the operators in quickly obtaining the basic information and controls needed for efficient operation of the laser system. The visible features

of the standard GUI can be seen in the Power Conditioning Executive GUI shown in Fig. 65.34 of Ref. 1.

The lower section of the screen features an infinitely scrollable (but clearable) window in which various operator messages are displayed. These messages are also logged to a file, for so-called *postmortem analysis,* should some error occur during operation of the laser system.

The upper portion of the screen features several standard displays and controls, including the clock time, time since last shot, database log number, executive title, and an abort button. These displays and controls are standard across the executives.

The center portion of the screen is used uniquely by each executive for its unique controls.

4. Broadcast
The broadcast interface is described in Ref. 1, p. 38.

5. LENA Interface
The LENA interface is described in Ref. 1, p. 38.

6. PLC's: Programmable Logic Controllers
Several of the subsystems use Programmable Logic Controllers (PLC's) as part of their construction. Several types are being used in the OMEGA system. Of these, two particular
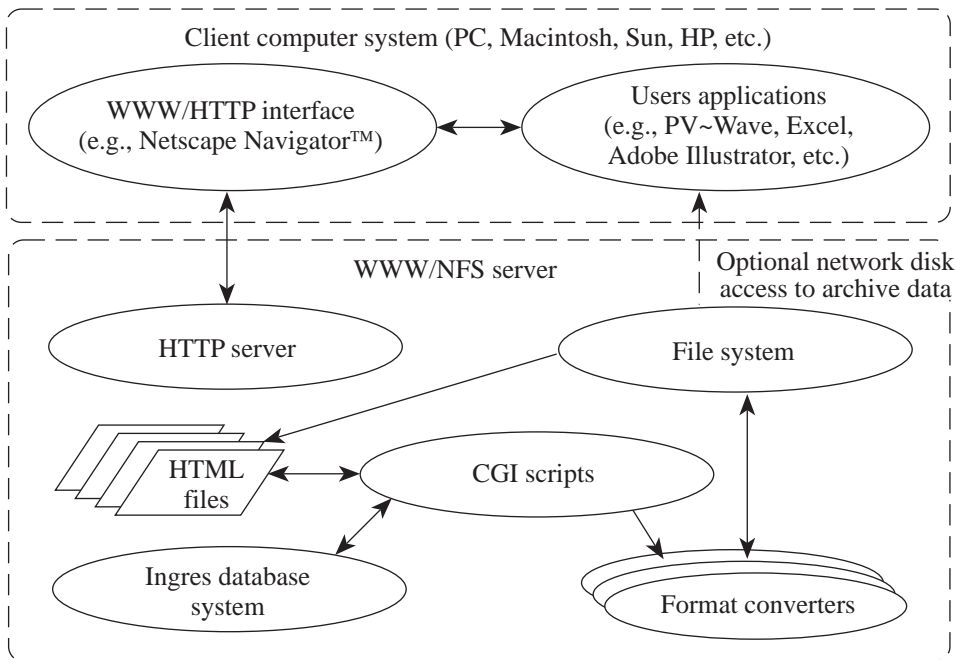

Figure 67.29
The LLE Image/Data archive is designed for easy access from throughout the Laboratory via World Wide Web interfaces such as Netscape Navigator™.

TC4180

PLC systems will be discussed: one produced by Square D, and another by GE Fanuc.

The Square D systems are being used in facility interlock and for control of the periscope mirror assembly (PMA), which is part of the ultraviolet (UV) alignment system and controlled through the Alignment Executive.

The GE Fanuc systems are used for main target vacuum and other target area controls (via the so-called HexPent[9] controllers), including the auxiliary vacuum systems, target positioner, and ten-inch manipulator (TIM) controls, as well as various target-area diagnostic system controls.

Generally, PLC's have been chosen in areas where inexpensive but highly reliable systems were desired for either local manual or automatic control of some subsystem.

Future Directions

Although the OMEGA laser system is now in operation and proceeding with its planned experiments, many aspects of the control system (several of which are outlined below) still remain to be developed or extended.

1. Automatic Alignment

The current system provides tools for alignment personnel to view the position of the laser beams, as well as control this position by adjusting the associated mirrors and other devices. In spite of this, given the large number of beams and even larger number of movable devices, it is unrealistic to expect humans to align the entire laser system within the 1-h shot cycle for which the system was designed. As a result, an automatic alignment system was envisioned where the measured beam positions would be folded back to produce computed moves so that the laser could be automatically aligned under software control.

Presently the position of the beams is measured and the mirrors are computer controlled, but closing this loop involves a substantial task of developing algorithms for computing the mapping of the beams' position to motor movement, as well as dealing with errors that can occur during the alignment process.

2. Templates

An important concept in the early design of the laser control system was the implementation of *templates*. These templates will provide predefined configurations for the laser and for both laser and experimental diagnostics for each shot.

A hierarchical scheme is envisioned for storing, merging, and verifying laser-device configuration, power-conditioning configuration, diagnostic configuration, and target chamber configuration, as well as recording this configuration after the shot.

At present, only limited portions of this system have been implemented, but as the system continues to evolve, we continue to move its design closer to this design goal.

3. On-Line Help

No system is complete without documentation. For the OMEGA laser, it is intended that most if not all of the documentation for the system will be available as on-line help, so that system operators will always have, at their fingertips, the facility to locate the information they need to answer any question about system operation.

To date, unfortunately, time and resources have not permitted the inclusion of this on-line help facility. When it is implemented, the current plan is to make use of the same World Wide Web interfaces that are being used for access to the image/data archive system. Some preliminary work along these lines has already begun.

4. Target Diagnostic Systems

Although they are not strictly part of the laser control system, a number of the target-area diagnostic systems are equally critical to safe and efficient operation of the laser as an experimental facility. As such, software for these systems is given equal priority and is currently under development.

5. Evolution

A goal of the upgrade of the OMEGA control system is a system that can grow and evolve with time. This goal was kept well in sight for this implementation, but much could be improved to prepare for the inevitable changes to come in computer systems and associated technology. As an example, as the POSIX.4 standard for lightweight processes becomes official and is supported, it would be prudent to convert the existing lightweight processes to this standard. Additional modularization and documentation of hardware-dependent subsystems would also be beneficial.

Summary

The control software for the OMEGA laser is composed of several major executives and supporting subsystems. Good design practices, including the use of both centralized and distributed control concepts, help keep the system manageable.

Cancellation of *B*-Integral Accumulation for CPA Lasers

Self-phase modulation (SPM) plays an important role in determining the final shape of the compressed pulse in chirped pulse amplification (CPA) lasers, even at relatively low values of the cumulative *B*-integral, $B \sim 1$ to 2.[1,2] The SPM distorts the linear chirp and causes the compressed pulse duration to increase noticeably near $B \sim 1$ and approximately double for $B \sim 2$.[1,2] It is possible to reset the expansion or compression gratings to compensate for this effect on average, but the radial variation of the *B*-integral means that it cannot be compensated for exactly. Temporal structure (wings) will unavoidably appear in a recompressed pulse, even for relatively small values of *B*.

We report the cancellation of the *B*-integral accumulated by a chirped pulse in a regenerative amplifier by using a GaAs plate that has a negative nonlinear index of refraction at 1.053 μm.[3] The absolute value of the nonlinear index of refraction is about three orders of magnitude larger than that of Nd:glass or KDP, so a thickness of less than 1 mm is required. We show that the compressed pulse duration and wings measured as a function of accumulated *B*-integral increase without the compensator plate as *B* exceeds 1, while with the GaAs plate installed the pulse duration remains fixed and the wings are reduced to almost their unmodulated value. The cancellation of the nonlinear phase was demonstrated with a 4.6-m Xe gas cell for a 10-ps KrF laser operating at 248.4 nm, which is just above two-photon resonance with the Xe $6p[1/2]_0$ state.[4]

1.053-μm chirped pulses are generated in a Nd:YLF oscillator coupled into a 0.8-km, single-mode fiber. They are subsequently expanded in a conventional single-grating, lens and mirror stretcher up to a 0.45-ns duration. One pulse is seeded into a *Q*-switched regenerative amplifier. Due to strong gain narrowing, the stretched pulse becomes Gaussian in time with a 0.3-ns duration.[5] As the pulse envelope builds up in the regenerative amplifier, the *B*-integral is accumulated on every pass. Near the peak of the *Q*-switched envelope the *B*-integral is approximately 0.18 per pass. By varying the switch-out time of the pulse relative to the peak of the pulse train, we vary the *B*-integral accumulated by the output pulse. The pulse passes through a pair of compression gratings, and the pulse duration is measured with an autocorrelator.

We modeled the regenerative amplifier using the Frantz-Novdik system of equations similar to Ref. 6 to estimate the cumulative *B*-integral. The round-trip loss factor is 50% due to the output coupler, and the 6.3% additional intracavity losses derived from equations are in good agreement with 55% measured with a cold cavity. The gain-narrowed pulse width is still slightly longer than the terminal-level lifetime of the active host. Although the final simulation values of output parameters are indistinguishable from the experimental ones, we still have 25% of systematic error and 10% random error in *B*-integral evaluation. The parameters of the regenerative amplifier are shown in Table 67.I.

A polished, 400-μm-thick, GaAs plate was inserted before the compression gratings to cancel the accumulated *B*-integral. To have a negative n_2 from the direct-beam semiconductor without strong single-photon absorption, the gap energy should be[3]
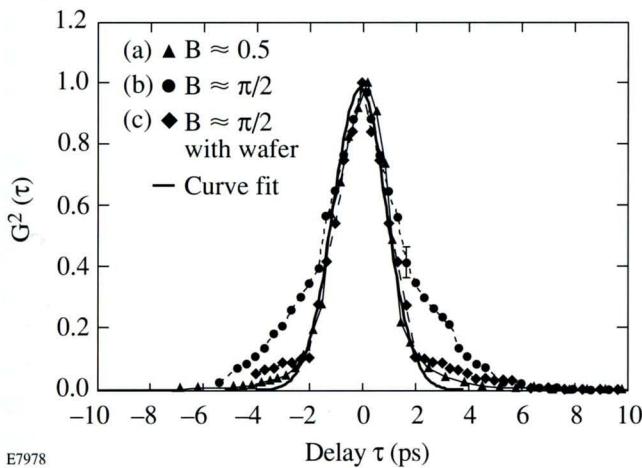
$$\hbar\omega < E_g < 1.42 \ \hbar\omega, \qquad (1)$$

where $\hbar\omega$ is the incident photon energy. The region of $x = \hbar\omega/E_g : 0.5 < x < 0.7$ can, in principle, be used for cancellation, but in that case the bound electronic contribution and the generated free-carrier contribution will have opposite signs, and the free-carrier contribution will be greatly reduced due to reduction of two-photon absorption coefficient that scales as[8] $\beta_2 \propto x^{-6}(2x-1)^{3/2}$. The nonlinear index of refraction of the GaAs plate estimated for 1.053 μm is -4.2×10^{-13} cm^2/W using an experimental value of -3.3×10^{-10} esu obtained for 1.064 μm[9] and scaling laws for $n_2(\hbar\omega/E_g)$.[3]

The power incident on the GaAs wafer was adjusted to cancel the accumulated *B*-integral and remove the temporal distortion of the compressed pulse (see Fig. 67.30). The 1.65-ps pulse generated with low accumulated *B*-integral (~ 0.5) is shown on trace (a). The pulse with time-bandwidth

Table 67.I: Parameters of Regenerative Amplifier

Active element	Q-98 Nd:phosphate glass, 6%; L = 115-mm athermal rod, ϕ = 7 mm; n_2 = 3.5 • 10^{-16} cm^2/W
Resonator	Stable $g \approx 1/2$, plano-concave, 100% end cavity dumped; 50% output flat; round-trip time 11.8 ns
Switch-in Q-switch Switch-out	external $\lambda/4$ and step $\lambda/4$ voltage to Pockels cell external
Saturation fluence[7]	4.7 J/cm^2
Round-trip, net small-signal gain	1.23
Seed fluence (J_{in}/J_{sat})	2 • 10^{-9}
Pump fluence (J_{sto}/J_{sat})	1.035
Peak fluence (without self-focusing)	0.146
Peak pass	86
Round-trip loss factor	0.437
Net gain Total gain	67 dB 363 dB
Waist on output coupler (w_0)	750 μm at low intensities and 500±50 μm at $B \sim \pi/2$

E7978

Figure 67.30
Experimentally measured autocorrelation of pulses compressed with (a) $B \approx$ 0.5; (b) $B \approx \pi/2$; and (c) $B \approx \pi/2$, accumulated in glass and canceled in the GaAs plate before compression.

product of 0.44±0.04 is generated by switching out the regenerative amplifier pulse 6 to 7 pulses before the peak of the Q-switched envelope. Pulses switched out at the peak of the Q-switched envelope have an accumulated B-integral of 1.6 (~$\pi/2$) and a compressed pulse duration of 2.0±0.1 ps [as shown in trace (b)]. They show significant non-Gaussian structure as expected.[1,2] Pulses compressed after passing

through the GaAs wafer are shown in trace (c). In this case, the pulse duration reduced to the original 1.65±0.1 ps with the structure significantly reduced. The wings at 5% of peak intensity level are due to higher-order phase aberrations in our CPA laser utilizing fiber[1] and not due to the regenerative amplifier.

Figure 67.31 shows the compressed pulse duration (FWHM) as a function of cumulative B-integral. The solid circles show that the pulse duration increases in the absence of cancellation, while the diamonds show that with cancellation, the pulse duration remains constant up to a B-integral of approximately $\pi/2$. The pulses in Fig. 67.31 have a slightly longer duration than those in Fig. 67.30 but are also transform limited. The graph from Fig. 67.31 with uncompensated pulses has a distinctive knee at B between 1 and 1.5 as expected.[1,2] A B-integral of 1 corresponds to an output intensity of 190 MW/cm^2. Internal losses for $B \approx \pi/2$ were near 10%.

The B-integral accumulated in the semiconductor can be found by solving the coupled intensity and free-generated carrier-density equations:[8]

$$\frac{dI(r,t,z)}{dz} = -\alpha I - \beta_2 I^2 - \sigma_{ex} NI, \qquad (2a)$$
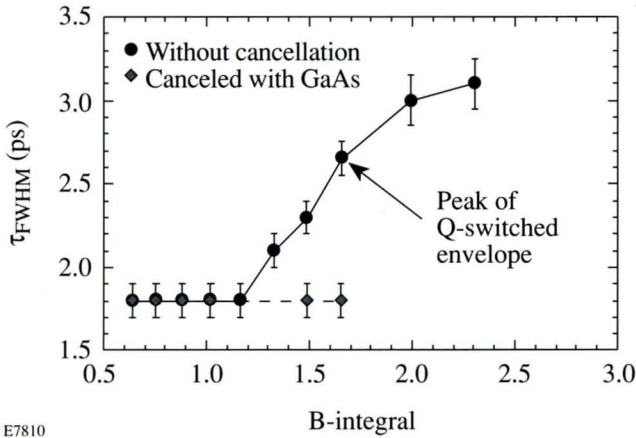
E7810

Figure 67.31
Pulse duration of switch-out pulses versus accumulated B-integral in the regenerative amplifier without subsequent cancellation in the GaAs plate (circles) and with subsequent cancellation in the GaAs plate (diamonds). The B-integral (x axis) has 25% systematic and 10% random error.

$$\frac{dN(r,t,z)}{dt} = -\frac{N(r,t,z)}{\tau_{\rm rel}} + \frac{\beta_2 I^2(r,t,z)}{2\hbar\omega}, \quad (2b)$$

$$\frac{dB(r,t,z)}{dz} = \frac{\omega}{c}(n_2 I - \sigma_r N). \quad (2c)$$

Here $\alpha = 2.3$ cm^{-1} and $\beta_2 = 20$ cm/GW are the linear and two-photon absorption coefficients; $\sigma_{\rm ex}$ is the exited carrier-absorption cross section; $\tau_{\rm rel}$ is the characteristic relaxation time of exited carriers; n_2 is the nonlinear index of refraction caused by bound electrons; and σ_r is the change in index of refraction per unit of photoexited charge-carrier density, N:[9]

$$\sigma_r = \frac{2\pi \hbar^2 e^2 E_p}{n_0 E_g^{\,3} x^2 (1 - x^2)}. \quad (3)$$

The exited carrier absorption term $-\sigma_{\rm ex} NI$ can be neglected up to intensities[8] $I_{\rm cr} \approx 2\hbar\omega/[\sigma_{\rm ex}(1-R)\tau_{\rm FWHM}]$, which is ~1 GW/cm^2 where $R = 0.3$ is the reflectivity of the uncoated crystal and $\sigma_{\rm ex} = 5 \times 10^{-18}$ cm^2.

The B-integral at the exit plane of the wafer, $z = L$, can be written in two terms. The fast term is caused by bound electrons and is

$$B_{\rm bnd}(r,t) = \frac{2\pi\, n_2}{\lambda_{\rm vac}\beta_2} \cdot \ell n\big[1 + \beta_2 I_0(r,t)(1-R)L_{\rm eff}\big], \quad (4)$$

where $L_{\rm eff} = (1 - e^{-\alpha L})/\alpha$. The thickness of the crystal L was assumed to be much smaller than the confocal beam parameter. The dependence of $B_{\rm bnd}(r,t)$ on $I_0(r,t)$ allows effective cancellation of the B-integral, when $\beta_2 I_0(1-R)L_{\rm eff} \ll 1$ (0.15 for our case).

Free carriers lead to the slow term,

$$B_{\rm ex}(r,t) = -\frac{2\pi}{\lambda_{\rm vac}}\frac{\sigma_r \beta_2}{2\hbar\omega}$$
$$\int_0^L dz\, e^{-t/\tau_{\rm rel}} \left[\int_{-\infty}^t e^{-t'/\tau_{\rm rel}} I^2(r,z,t')dt'\right]. \quad (5)$$

The relaxation time $\tau_{\rm rel}$ is estimated to be ~100 ps — about one third of the laser-pulse duration.[10] The free-carrier nonlinearity $\sigma_r N$ is proportional to a temporal integral of I^2 and cannot compensate for the accumulated B-integral in glass for long relaxation times $\tau_{\rm rel} \gtrsim \tau_p$. Moreover, for intensities higher than ~20 MW/cm^2 this term becomes comparable to $B_{\rm bnd}$ and exceeds $B_{\rm bnd}$ by more than an order of magnitude for $I_{\rm inc} \approx 1$ GW/cm^2 with laser-pulse duration $\tau_{\rm FWHM} \approx \tau_{\rm rel}$. However, for a relaxation time of one third of the pulse width, the contribution from the two terms is comparable at sub GW/cm^2 intensities. For short relaxation times ($\tau_{\rm rel} \ll \tau_p$), $B_{\rm ex}$ follows the intensity dependence as well.

The B-integral of the pulses incident onto the GaAs crystal was taken as $B_{\rm glass}(r,t) = B_{\rm glass} \cdot I_0(r,t)/I_0(0,0)$, where $B_{\rm glass}$ is the peak B-integral accumulated in the regenerative amplifier. The total accumulated integral $B_{\rm tot}(r,t)$ after the GaAs crystal,

$$B_{\rm tot}(r,t) = B_{\rm glass}(r,t) + B_{\rm bnd}(r,t) + B_{\rm ex}(r,t), \quad (6)$$

can be reduced to values allowing wingless compression of the pulse for appropriate beam and crystal parameters. Figure 67.32 shows a calculation of $B_{\rm tot}(0,t)$ and $B_{\rm tot}(r,0)$ for a laser pulse that is Gaussian in time and space,

$$I_0(r,t) = I_0 \exp\Big[-2(r/w_0)^2 - 4\ln 2(t/\tau_{\rm FWHM})^2\Big],$$

with $I_0 = 285$ MW/cm^2 and $\sigma_r = 5.4 \times 10^{-21}$ cm^3 (calculated
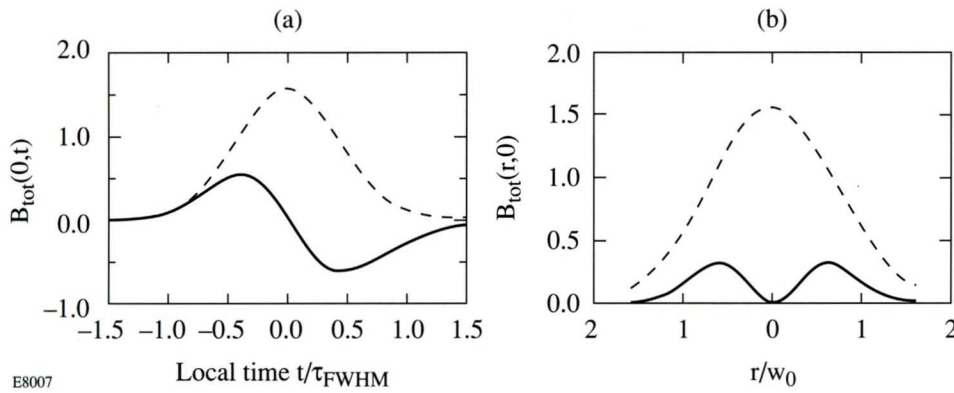
Figure 67.32
Theoretically estimated residual phase after accumulation of the $B \approx \pi/2$ in absorptionless material (dashed line) (pure positive n_2) and cancellation in GaAs (solid line) with $\alpha = 2.3$ cm^{-1}, $\beta_2 = 20$ cm/GW, $n_2 = -4.2 \times 10^{-13}$ cm^2/W, $\sigma_r = 5.4 \times 10^{-21}$ cm^3, $L = 400$ μm, $I_{inc,0} = 285$ MW/cm^2, $R = 0.3$ ($n = 3.47$), with duration of stretched pulse $\tau_{FWHM} = 300$ ps and $\tau_{rel} = \tau_{FWHM}/3$: (a) radial profile at the temporal peak of the pulse, (b) temporal profile though the axis of the beam.

for $E_g = 1.4$ eV and $\hbar\omega = 1.177$ eV).[9] The intensity was chosen so that $-B_{bnd}(0,0) - B_{ex}(0,0) = B_{glass}(0,0) = \pi/2$. The cancellation reduced the B-integral to a temporal maximum of 0.5 and 0.3 radially at the temporal peak of the pulse. The computation shows that for a slightly longer crystal and smaller intensities the B-integral can be reduced by another factor of 2. The optimal choice of low-temperature (LT)-grown semiconductors with special dopants and/or longer pulses can reduce the τ_{rel}/τ_{laser} ratio and allow reduction of the B-integral to negligible values. The estimated dispersion (wavelength dependence) of α, β_2, or n_2 is negligible for a 10-Å spectrum.

AlGaAs with $E_g = 1.57$ eV has the same properties for $\lambda \approx 850$ nm —$\alpha = 1$ cm^{-1}, $n_2 \approx -5 \times 10^{-13}$ cm^2/W (Ref. 11), $\sigma_r \approx 5 \times 10^{-21}$ cm^3, and $\beta_2 = 10$ cm/GW— as GaAs at 1.053 μm. However, for $x \approx 0.92$ one should take into account the wavelength dependence (i.e., dispersion) of these parameters for efficient compensation of the B-integral.

The spatial B-integral accumulated in high-power lasers can be precompensated by placing a semiconductor wafer somewhere upstream in the laser path. Aside from coupling (fresnel) losses, which can be removed by an appropriate AR

coating, linear and TPA losses should be small enough for sufficient B-integral accumulation to justify placing the semiconductor for cancellation. The conditions $\alpha L \ll 1$, $\beta_2\, IL_{eff} < 1$, and $B = (2\pi/\lambda)\Delta n L_{eff}$ are the same as those used in all optical-switching inequalities.[12] These inequalities ($n_2/\beta_2\lambda > B/2\pi$, $\Delta n/\alpha\lambda > B/2\pi$) are satisfied for B as large as π due to fairly large nonlinearities of GaAs for a fixed wavelength. For our case the bound electronic contribution is $n_2/\beta_2\lambda = 0.2$, and free-carrier index change is comparable to that caused by bound electrons.

Thus, the same semiconductor technique can be used to cancel the radially dependent B-integral acquired due to a nonuniform intensity profile in a long-pulse, high-power laser system. The wafer can be used as a pre- or post-compensator, depending on experimental conditions. Because the accumulated positive B-integral in the amplifier and the negative B-integral in the wafer are both proportional to the intensity, input intensity fluctuations do not affect the quality of cancellation.

The simulation in Fig. 67.33 shows cancellation of spatial and temporal B-integral with a GaAs wafer. A supergaussian in space ($n = 8$) and Gaussian in time ($\tau_{FWHM} = 1$ ns) pulse
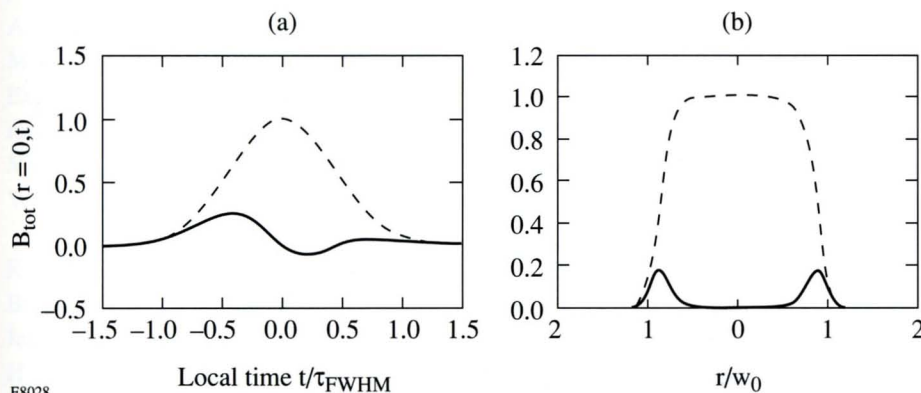

Figure 67.33
Theoretically estimated residual phase after the propagation of a 1-ns pulse with an incident peak B-integral of unity before (dashed line) and after (solid line) GaAs plate with $\alpha = 1$ cm^{-1}, $L = 2$ mm, $I_{inc,0} = 90$ MW/cm^2, $\tau_{rel} = \tau_{FWHM}/10$: (a) radial profile at the temporal peak of the pulse; (b) temporal profile though the axis of the beam.

with peak intensity incident onto GaAs wafer I_0 (0,0) = 90 MW/cm^2 has a pre-accumulated B-integral of 1. This pulse is close to ~3 times the expanded LARA output beam.[13] All parameters of the GaAs wafer were the same as above except the thickness, which was 2 mm, and the linear absorption coefficient $\alpha = 1$ cm^{-1}. The phase accumulated after the cancellation is more than five times smaller than the initial phase and represents reduction of the phase error from $\lambda/6$ to $\lambda/30$. A 10% incident-energy fluctuation results in variation of residual phase by $\left| \delta B_{max} \right| \approx 0.08$.

In conclusion we have demonstrated for the first time that the nonlinear phase can be canceled in CPA lasers by using a semiconductor with negative nonlinear index of refraction.

ACKNOWLEDGMENT

REFERENCES

1. Y.-H. Chuang, L. Zheng, and D. D. Meyerhofer, IEEE J. Quantum Electron. **29**, 270 (1993).

2. M. D. Perry, T. Ditmire, and B. C. Stuart, Opt. Lett. **19**, 2149 (1994).

3. M. Sheik-Bahae et al., IEEE J. Quantum Electron. **27**, 1296 (1991).

4. R. H. Lehmbert et al., Opt. Commun. **121**, 78 (1995).

5. Y.-H. Chuang, D. D. Meyerhofer, S. Augst, H. Chen, J. Peatross, and S. Uchida, J. Opt. Soc. Am. B **8**, 1226 (1991).

6. F. P. Strohkendl, D. J. Files, and L. R. Dalton, J. Opt. Soc. Am. B **11**, 742 (1994).

7. S. E. Stokowski, R. A. Saroyan, and M. J. Weber, Lawrence Livermore National Laboratory Report, M-095, Rev. 2 (1981), Vol. 1, p. 10.

8. E. W. Van Stryland et al., Opt. Eng. **24**, 613 (1985).

9. A. A. Said et al., J. Opt. Soc. Am. B **9**, 405 (1992).

10. W. Donaldson, private communication.

11. M. J. LaGasse et al., Appl. Phys. Lett. **56**, 417 (1990).

12. V. Mizrahi et al., Opt. Lett. **14**, 1140 (1989).

13. Laboratory for Laser Energetics LLE Review **58**, NTIS document No. DOE/SF/19460-17, 1994 (unpublished), p. 90.

A set of semi-autonomous processes called Executives perform the major control functions, with the help of several interface and support programs.

Implemented in C/C++ and making use of X/Motif and *threads,* these programs take best advantage of state-of-the-art software tools to provide an efficient and effective interface for the power conditioning hardware. Graphical User Interfaces make the system easy to operate and present the status of the system in an attractive and accessible format.

To perform their tasks, the various Executives interact continuously with a central database system, a master timing interface, other Executives, the Neuron™-based control modules, and various other devices. Judicial use of *threads,* or *lightweight processes*, and interprocess communication allows these many tasks to be performed in concert with one another.

The successful deployment of this control system, as part of the entire OMEGA Upgrade Project, has been the work of many individuals over several years. Many more years of work remain to implement all desired aspects of this new OMEGA laser control system.

ACKNOWLEDGMENT

REFERENCES

1. Laboratory for Laser Energetics LLE Review **65**, NTIS document No. DOE/SF/19460-117, 1995 (unpublished).

2. IEEE Std. 1003.1, *Information Technology–Portable Operating System Interface (POSIX)–Part 1: System Application Programming Interface (API)*, 1st ed. (IEEE, New York, 1990).

3. IEEE Std. 1003.2, *Standard for Information Technology–Portable Operating System Interface (POSIX)–Part 2: Shell and Utilities* (IEEE, New York, 1992), Vol. 2.

4. B. W. Kernighan and D. M. Richie, *The C Programming Language*, 2nd ed. (Prentice Hall, Englewood Cliffs, NJ, 1988).

5. B. Stroustrup, *The C++ Programming Language*, 2nd ed. (Addison Wesley, Reading, MA, 1991).

6. PV-WAVE™ is a registered trademark of Precision Visuals, Inc. It is an interactive environment for data analysis and plotting.

7. A GUI builder is a tool and environment for interactive construction of GUI's.

8. The Neuron™ name is a trademark for single-chip, network-based microcontrollers produced by Echelon Corporation.

9. The HexPent controllers are so-named because of the hexagon and pentagon formation of each functional section of the target chamber support structure.

Publications and Conference Presentations

Publications

R. Betti, V. N. Goncharov, R. L. McCrory, P. Sorotokin, and C. P. Verdon, "Self-Consistent Stability Analysis of Ablation Fronts in Inertial Confinement Fusion," Phys. Plasmas **3**, 2122 (1996) (invited).

J. D. B. Featherstone, D. Fried, S. M. McCormack, and W. Seka, "Effect of Pulse Duration and Repetition Rate on CO_2 Laser Inhibition of Caries Progression," in *Lasers in Dentistry II* (SPIE, Bellingham, WA, 1996), Vol. 2672, pp. 79–87.

D. Fried, J. D. B. Featherstone, S. R. Visuri, W. Seka, and J. T. Walsh, "The Caries Inhibition Potential of Er:YAG and Er:YSGG Laser Radiation," in *Lasers in Dentistry II* (SPIE, Bellingham, WA, 1996), Vol. 2672, pp. 73–78.

R. S. Marjoribanks, F. W. Budnik, H. Chen, and D. D. Meyerhofer, "Electron Temperature in Transient Plasmas from Quasi-Steady Ratio of Isoelectronic Lines: Application to Picosecond and Subpicosecond Plasmas," J. Opt. Soc. Am. B **13**, 380 (1996).

R. L. McCrory, J. M. Soures, C. P. Verdon, T. R. Boehly, D. K. Bradley, R. S. Craxton, J. A. Delettrez, R. Epstein, P. A. Jaanimagi, S. D. Jacobs, R. L. Keck, J. H. Kelly, T. J. Kessler, H. Kim, J. P. Knauer, R. L. Kremens, S. A. Kumpan, S. A. Letzring, F. J. Marshall, P. W. McKenty, S. F. B. Morse, A. Okishev, W. Seka, R. W. Short, M. D. Skeldon, S. Skupsky, M. Tracy, and B. Yaakobi, "Direct-Drive Laser Fusion Experimental Program at the University of Rochester's Laboratory for Laser Energetics," in *Plasma Physics and Controlled Nuclear Fusion Research 1994* (IAEA, Vienna, 1996), Vol. 3, pp. 33–37.

R. L. McCrory, J. M. Soures, C. P. Verdon, T. R. Boehly, D. K. Bradley, R. S. Craxton, J. A. Delettrez, R. Epstein, P. A. Jaanimagi, S. D. Jacobs, R. L. Keck, J. H. Kelly, T. J. Kessler, H. Kim. J. P. Knauer, R. L. Kremens, S. A. Kumpan, S. A. Letzring, F. J. Marshall, P. W. McKenty, S. F. B. Morse, A. Okishev, W. Seka, R. W. Short, M. D. Skeldon, S. Skupsky, M. Tracy, and B. Yaakobi, "Experiments on the OMEGA Laser to Validate High-Gain, Direct-Drive Performance on the National Ignition Facility," in *Laser Interaction and Related Plasma Phenomena*, edited by S. Nakai and G. H. Miley (American Institute of Physics, Woodbury, NY, 1996), Vol. 369, pp. 71–79.

C. J. McKinstrie, J. S. Li, R. E. Giacone, and H. X. Vu, "Two-Dimensional Analysis of the Power Transfer Between Crossed Laser Beams," Phys. Plasmas **3**, 2686 (1996).

D. Ofer, U. Alon, D. Shvarts, R. L. McCrory, and C. P. Verdon, "Modal Model for the Nonlinear Multimode Rayleigh-Taylor Instability," Phys. Plasmas **3**, 3073 (1996).

S. Papernov and A. W. Schmid, "A Comparison of Laser-Induced Damage Morphology in Three Model Thin-Film Systems: HfO_2, Y_2O_3, and Ta_2O_5," in *Laser-Induced Damage in Optical Materials: 1994*, edited by M. R. Kozlowski, A. H. Guenther, B. E. Newnam, H. E. Bennett, and M. J. Soileau (SPIE, Bellingham, WA, 1995), Vol. 2428, pp. 385–396.

W. Seka, J. D. B Featherstone, D. Fried, S. R. Visuri, and J. T. Walsh, "Laser Ablation of Dental Hard Tissue: From Explosive Ablation to Plasma-Mediated Ablation," in *Lasers in Dentistry II*, edited by J. Neev, H. A. Wigdor, J. M. White, and J. D. Featherstone (SPIE, Bellingham, WA, 1996), Vol. 2672, pp. 144–158 (invited).

J. M. Soures, R. L. McCrory, C. P. Verdon, A. Babushkin, R. E. Bahr, T. R. Boehly, R. Boni, D. K. Bradley, D. L. Brown, R. S. Craxton, J. A. Delettrez, W. R. Donaldson, R. Epstein, P. A. Jaanimagi, S. D. Jacobs, K. Kearney, R. L. Keck, J. H. Kelly, T. J. Kessler, R. L. Kremens, J. P. Knauer, S. A. Kumpan, S. A. Letzring, D. J. Lonobile, S. J. Loucks, L. D. Lund, F. J.

Marshall, P. W. McKenty, D. D. Meyerhofer, S. F. B. Morse, A. Okishev, S. Papernov, G. Pien, W. Seka, R. Short, M. J. Shoup III, M. Skeldon, S. Skupsky, A. W. Schmid, D. J. Smith, S. Swales, M. Wittman, and B. Yaakobi, "Direct-Drive Laser-Fusion Experiments with the OMEGA, 60-Beam, >40-kJ, Ultraviolet Laser System," Phys. Plasmas **3**, 2108 (1996) (invited).

B. Yaakobi, R. S. Craxton, R. Epstein, and Q. Su, "Diagnosis of Core-Shell Mixing Using Absorption and Emission Spectra of a Doped Layer," J. Quant. Spectrosc. Radiat. Transf. **55**, 731 (1996).

B. Yaakobi, R. Epstein, C. F. Hooper, Jr., D. A. Haynes, Jr., and Q. Su, "Diagnosis of High-Temperature Implosions Using Low- and High-Opacity Krypton Lines," J. X-Ray Sci. Technol **6**, 172 (1996).

Forthcoming Publications

E. L. Alfonso, S.-H. Chen, M. D. Wittman, S. Papernov, and D. Harding, "A Parametric Study of Microencapsulation Approach to the Preparation of Polystyrene Shells," to be published in Polymer.

T. R. Boehly, D. L. Brown, R. S. Craxton, R. L. Keck, J. P. Knauer, J. H. Kelly, T. J. Kessler, S. A. Kumpan, S. J. Loucks, S. A. Letzring, F. J. Marshall, R. L. McCrory, S. F. B. Morse, W. Seka, J. M. Soures, and C. P. Verdon, "Initial Performance Results of the OMEGA Laser System," to be published in Optics Communications.

S.-H. Chen, J. C. Mastrangelo, T. N. Blanton, A. Bashir-Hashemi, and K. L. Marshall, "Novel Glass-Forming Liquid Crystals. IV. Effects of Central Core and Pendant Group on Vitrification and Morphological Stability," to be published in Liquid Crystals.

S.-H. Chen, H. Shi, J. C. Mastrangelo, and J. J. Ou, "Thermotropic Chiral Nematic Side-Chain Polymers and Cyclic Oligomers," to be published in Progress in Polymer Science.

S.-H. Chen, H. Shi, B. M. Conger, J. C. Mastrangelo, and T. Tsutsi, "Novel Vitrifiable Liquid Crystals as Optical Materials," to be published in Advanced Materials.

A. V. Chirokikh, W. Seka, A. Simon, and R. S. Craxton, "Brillouin Scattering in Long-Scale-Length Laser Plasmas," to be published in Physics of Plasmas.

C. T. Cotton, "The Design of an All-Spherical, Three-Mirror, Off-Axis Telescope Objective," to be published in the OSA Proceedings of the International Optical Design Conference '94, Rochester, NY.

P. M. Fauchet, "Photoluminescence and Electroluminescence from Porous Silicon," to be published in the Journal of Photoluminescence (invited).

P. M. Fauchet, "Porous Silicon: Photoluminescence and Electroluminescent Devices," to be published in Light Emission in Silicon, Semiconductors, and Semimetals Series.

D. Fried, R. E. Glena, J. D. B. Featherstone, and W. Seka, "Permanent and Transient Changes in the Reflectance of CO_2 Laser-Irradiated Dental Hard Tissues at $\lambda = 9.3, 9.6, 10.3$, and 10.6 μm and at Fluences between 1–20 J/cm^2," to be published in Lasers in Surgery and Medicine.

D. Golini, Y. Zhou, S. D. Jacobs, F. Yang, D. Quesnel, C. Gracewski, M. Atwood, and E. Fess, "Aspheric Surface Generation Requirements in Magnetorheological Finishing," to be published in Trends in Optics & Photonics (TOPS).

V. N. Goncharov, R. Betti, R. L. McCrory, and C. P. Verdon, "Self-Consistent Stability Analysis of Ablation Fronts with Small Froude Numbers," to be published in Physics of Plasmas.

J. H. Kelly, T. R. Boehly, J. M. Soures, D. L. Brown, R. Boni, R. S. Craxton, R. L. Keck, T. J. Kessler, R. Kremens, S. A. Kumpan, S. A. Letzring, S. J. Loucks, R. L. McCrory, S. F. B. Morse, W. Seka, S. Skupsky, and C. P. Verdon, "The Activation of the Upgraded OMEGA Laser at the University of Rochester," to be published in the SPIE Proceedings of the 15th International Conference on Coherent and Nonlinear Optics, St. Petersburg, Russia, June 1995.

J. H. Kelly, T. R. Boehly, J. M. Soures, D. L. Brown, R. Boni, R. S. Craxton, R. L. Keck, T. J. Kessler, R. L. Kremens, S. A. Kumpan, S. A. Letzring, S. J. Loucks, R. L. McCrory, S. F. B. Morse, W. Seka, S. Skupsky, and C. P. Verdon, "The Activation of the Upgraded OMEGA Laser at the University of Rochester," to be published in the SPIE Proceedings of the 1st Annual International Conference on Solid-State Lasers for Application to Inertial Confinement Fusion (ICF), Monterey, CA, 30 May–2 June 1995.

T. J. Kessler, L. S. Iwan, J. Barone, C. Kellogg, and W. P. Castle, "Optic Fabrication Using Photographic Lithography," to be published in the Bulletin of the American Physical Society.

E. M. Korenic, S. D. Jacobs, S. M. Faris, and L. Li, "Colorimetry of Cholesteric Liquid Crystals," to be published in the Bulletin of the American Physical Society.

K. S. Lebedev, E. A. Magulariya, S. G. Lukishova, S. V. Belyaev, N. V. Malimonenko, and A. W. Schmid, "Reflective Nonlinearities of Nonabsorbing Chiral Liquid Crystals: Frustration of Selective Reflection by Powerful Laser Radiation," to be published in the Bulletin of the American Physical Society.

Y. Lin, T. J. Kessler, and G. N. Lawrence, "Design of Continuous Surface-Relief Phase Plates by Simulated Annealing to Achieve Control of Focal Plane Irradiance," to be published in Optics Letters.

S. G. Lukishova, S. V. Belyaev, K. S. Lebedev, E. A. Magulariya, A. W. Schmid, and N. V. Malimonenko, "cw and High-Repetition-Rate Lasing in Nd:YAG Resonators with Chiral-Nematic Liquid-Crystal Mirrors: A Study of Nonlinear Responses," to be published in Quantum Electronics.

S. G. Lukishova, S. V. Belyaev, K. S. Lebedev, E. A. Magulariya, A. W. Schmid, and N. V. Malimonenko, "Nonlinear Bleaching in the Selective Reflection of Nonabsorbing Chiral-Nematic Liquid-Crystal Thin Films," to be published in JETP Letters and in Molecular Crystals and Liquid Crystals.

J. C. Mastrangelo and S.-H. Chen, "Novel Glass-Forming Organic Materials. 2. Cyclohexane and Bicyclooctene with Pendant Pyrenene and Carbazole," to be published in Chemistry of Materials.

S. M. McCormack, D. Fried, J. D. B. Featherstone, R. E. Glena, and W. Seka, "Scanning Electron Microscope Observations of CO_2 Laser Effects on Dental Enamel," to be published in the Journal of Dental Research.

C. J. McKinstrie and E. A. Startsev, "Electron Acceleration by a Laser Pulse in a Plasma," to be published in Physical Review E.

A. Okishev, M. D. Skeldon, S. A. Letzring, W. R. Donaldson, A. Babushkin, and W. Seka, "The Pulse-Shaping System for the 60-Beam, 30-kJ (UV) OMEGA Laser," to be published in the Proceedings of Laser Optics '95 Conference, St. Petersburg, Russia, 27 June–1 July 1995.

J. Z. Roach, A. Ninkov, S. W. Swales, and T. Morris, "Design and Evaluation of a Screen CCD Imaging System," to be published in Optical Engineering.

A. W. Schmid, T. J. Kessler, S. Papernov, and J. Barone, "Low-Surface-Energy Photoresist as a Medium for Optical Replication," to be published in Applied Physics Letters.

J. D. Schnittman and R. S. Craxton, "Indirect-Drive Radiation Uniformity in Tetrahedral Hohlraums," to be published in Physics of Plasmas.

A. Simon, "Comparison Between SBS Theories and Experiment," to be published in Proceedings of the LaJolla Summer School '95, Plasma Physics and Technology (AIP).

J. M. Soures, S. J. Loucks, R. L. McCrory, C. P. Verdon, A. Babushkin, R. E. Bahr, T. R. Boehly, R. Boni, D. K. Bradley, D. L. Brown, J. A. Delettrez, R. S. Craxton, W. R. Donaldson, R. Epstein, R. Gram, D. R. Harding, P. A. Jaanimagi, S. D. Jacobs, K. Kearney, R. L. Keck, J. H. Kelly, T. J. Kessler, R. L. Kremens, J. P. Knauer, S. A. Letzring, D. J. Lonobile, L. D. Lund, F. J. Marshall, P. W. McKenty, D. D. Meyerhofer, S. F. B. Morse, A. Okishev, S. Papernov, G. Pien, W. Seka, R. W. Short, M. J. Shoup, III, M. D. Skeldon, S. Skupsky, A. W. Schmid, D. J. Smith, S. Swales, M. D. Wittman, and B. Yaakobi, "The Role of the Laboratory for Laser Energetics in the National Ignition Facility Project," to be published in Fusion Technology.

M. D. Wittman, R. Q. Gram, H. Kim, C. K. Immesoete, S. G. Noyes, and S. Scarantino, "Increased Retention Time for

Hydrogen and Other Gases by Polymer Shells Using Optically Transparent Aluminum Layers," to be published in the Journal of Vacuum Science and Technology.

W. Xiong, Y. Kostoulas, X. Weng, P. M. Fauchet, and R. Sobolewski, "Femtosecond Study of the Electronic Structure in Semiconducting Y-Ba-Cu-O," to be published in Physical Review B.

B. Yaakobi, F. J. Marshall and J. A. Delettrez, "Abel Inversion of Cryogenic Laser Target Images," to be published in Optics Communications.

B. Yaakobi, F. J. Marshall, and R. Epstein, "High Temperature of Laser-Compressed Shells Measured with Kr^{+34} and Kr^{+25} X-Ray Lines," to be published in Physical Review E.

J. D. Zuegel and W. Seka, "Direct Measurements of Lower-Level Lifetime in Nd:YLF," to be published in the Bulletin of the American Physical Society.

J. D. Zuegel and W. Seka, "Upconversion and Reduced $^4F_{3/2}$ Upper-State Lifetime in Intensely Pumped Nd:YLF," to be published in Optics Letters.

Conference Presentations

The following presentations were made at the Materials Research Society 1996 Spring Meeting, San Francisco, CA, 8–12 April 1996:

B. M. Conger, H. Shi, S.-H. Chen, and T. Tsutsui, "Polarized Fluorescence from Vitrified Liquid Crystalline Films."

S.-H. Chen, H. Shi, B. M. Conger, D. Katsis, and J. C. Mastrangelo, "Novel Vitrified Liquid Crystals and Potential Applications."

J. C. Mastrangelo, S.-H.Chen, T. N. Blanton, and A. Bashir-Hashemi, "Vitrification and Morphological Stability of Liquid Crystals."

H. Shi, D. Katsis, and S.-H. Chen, "Dynamics of Defect Annihilation in Vitrified Liquid Crystalline (VLC) Thin Films."

H. Shi and S.-H. Chen, "Theory of Circularly Polarized Emission from Chiral Nematic Liquid Crystalline Films."

The following presentations were made at the OSA Topical Meeting on Optical Fabrication and Testing, Boston, MA, 29 April–3 May 1996:

B. E. Gillman, S. D. Jacobs, and S. E. Snyder, "New Developments in Bound Abrasive Polishing of Optical Glass on Opticam(R) Machining Centers."

S. D. Jacobs, E. Fess, B. E. Gillman, H. Edwards, D. Golini, W. I. Kordonski, V. W. Kordonski, I. Prokhorov, and F. Yang, "Magnetorheological Fluid Composition and Enhanced Material Removal Rates with Nanodiamonds."

W. I. Kordonski, S. D. Jacobs, D. Golini, E. Fess, D. Strafford, J. Ruckman, and M. Bechtold, "Vertical Wheel Magnetorheological Finishing Machine for Flat, Convex, and Concave Surfaces."

J. Lambropoulous, F. Yang, and S. D. Jacobs, "Toward a Mechanical Mechanism for Material Removal in Magnetorheological Finishing."

D. Golini, Y. Zhou, S. D. Jacobs, F. Yang, D. Quesnel, C. Gracewski, M. Atwood, and E. Fess, "Aspheric Surface Generation Requirements in Magnetorheological Finishing."

The following presentations were made at the 11th Topical Conference on High-Temperature Plasma Diagnostics, Monterey, CA, 12–16 May 1996:

B. DeMarco, C. W. Barnes, K. Kearney, and R. L. Kremens, "Neutron Yield Measurement on the OMEGA Laser System."

R. L. Kremens, J. T. Canosa, D. L. Brown, T. H. Hinterman, M. Litchfield, D. Lonobile, R. G. Roides, M. Thomas, and R. Weaver, "The OMEGA Laser Electronic Timing System."

F. J. Marshall and J. A. Oertel, "A Framed Monochromatic X-Ray Microscope for ICF."

The following presentations were made at the 1996 Annual Meeting of the Division of Atomic, Molecular, and Optical Physics, Ann Arbor, MI, 15–18 May 1996:

M. S. Adams and D. D. Meyerhofer, "Spatial Coherence of Third Harmonic Produced by High-Intensity Interaction in a Noble Gas."

B. Buerke, J. P. Knauer, S. J. McNaught, C. I. Moore, and D. D. Meyerhofer, "Precise Test of Tunneling Theories by the Laser Ionization of Hydrogenic Helium."

S. J. McNaught, J. P. Knauer, and D. D. Meyerhofer, "Measurements of the ac Tunneling Ionization Phase with a Linearly Polarized, High-Intensity Laser."

D. D. Meyerhofer, J. P. Knauer, S. J. McNaught, and C. I. Moore, "Observation of Relativistic Mass Shift Effects during High-Intensity Laser-Electron Interactions."

The following presentations were made at OSA's Tenth International Topical Meeting on Ultrafast Phenomena, San Diego, CA, 28 May–1 June 1996:

P. M. Fauchet, Ju. V. Vandyshev, Z. Xu, C. W. Rella, H. A. Schwettman, and G. W. Wicks, "Mid-Infrared Femtosecond Spectroscopy of Intersubband Hot-Hole Relaxation in Quantum Wells."

O. A. Konoplev and D. D. Meyerhofer, "Cancellation of B-Integral Accumulation in CPA Lasers."

Z. Xu, Ju. V. Vandyshev, P. M. Fauchet, C. W. Rella, H. A. Schwettman, and C. C. Tsai, "Ultrafast Excitation and De-excitation of Local Vibrational Modes in a Solid Matrix: The Si-H Bond in Amorphous Silicon."

The following presentations were made at CLEO/QELS '96, Anaheim, CA, 2–7 June 1996:

A. Babushkin, W. Bittle, S. A. Letzring, A. Okishev, W. Skeldon, and W. Seka, "Stable, Reproducible, and Externally Synchronizable Regenerative Amplifier for Shaped Optical Pulses for the OMEGA Laser System."

T. R. Boehly, R. S. Craxton, P. A. Jaanimagi, R. L. Keck, J. H. Kelly, T. J. Kessler, R. L. Kremens, S. A. Kumpan, S. A.

Letzring, R. L. McCrory, S. F. B. Morse, W. Seka, S. Skupsky, J. M. Soures, M. D. Tracy, and C. P. Verdon, "Irradiation Uniformity Studies and Fusion Experiments on the OMEGA Laser Facility."

M. J. Guardalben, "Off-Line Tuning of KDP Frequency Conversion Crystals for the Laboratory for Laser Energetics' 60-Beam OMEGA Laser."

J. H. Kelly, R. L. Keck, T. J. Kessler, S. A. Letzring, S. Skupsky, D. L. Brown, T. A. Safford, W. Seka, A. Babushkin, T. R. Boehly, P. A. Jaanimagi, A. Okishev, and S. F. B. Morse, "Performance of the OMEGA Nd:Glass Laser System" (invited).

O. A. Konoplev and D. D. Meyerhofer, "Cancellation of B-Integral Accumulation in CPA Lasers."

A. Okishev, M. D. Skeldon, S. A. Letzring, R. Boni, and W. Seka, "Comparative Investigation of Fast Photodetector Responses to Complex Shaped Optical Pulses."

The following presentations were made at the 24th European Conference on Laser Interaction with Matter (24th ECLIM), Madrid, Spain, 3–7 June 1996:

R. Betti, V. N. Goncharov, R. L. McCrory, and C. P. Verdon, "Linear Theory of the Ablative-Rayleigh Taylor Instability."

R. L. McCrory, "The LLE Direct-Drive Target Physics Experimental Program: First Year of ICF Experiments on OMEGA" (invited).

S. D. Jacobs, B. E. Gillman, J. C. Lambropoulos, T. Fang, Y. Zhou, D. Golini, and M. Atwood, "The Effect of the Coolant on the Glass Work and the Diamond Tool in Deterministic Microgrinding," ASPE Spring Topical Meeting on Precision Grinding of Brittle Materials, Annapolis, MD, 3–6 June 1996.

J. Z. Roach and S. W. Swales, "A Network-Based Imaging System for the OMEGA Laser System," European Symposium on Lasers, Optics, and Vision for Productivity in Manufacturing I, Micropolis, Besancon, France, 10–14 June 1996.

The following presentations were made at the 12th Topical Meeting on the Technology of Fusion Energy, Reno, NV, 16–20 June 1996:

J. P. Knauer, S. J. Loucks, R. L. McCrory, J. M. Soures, C. P. Verdon, A. Babushkin, R. E. Bahr, T. R. Boehly, R. Boni, D. K. Bradley, D. L. Brown, J. A. Delettrez, R. S. Craxton, W. R. Donaldson, R. Epstein, R. Q. Gram, D. R. Harding, P. A. Jaanimagi, S. D. Jacobs, K. Kearney, R. L. Keck, J. H. Kelly, T. J. Kessler, R. L. Kremens, S. A. Letzring, D. J. Lonobile, L. D. Lund, F. J. Marshall, P. W. McKenty, D. D. Meyerhofer, S. F. B. Morse, A. Okishev, S. Papernov, G. Pien, W. Seka, R. W. Short, M. J. Shoup III, M. D. Skeldon, S. Skupsky, A. W. Schmid, D. J. Smith, S. Swales, M. D. Wittman, and B. Yaakobi, "Recent Experimental Results from the OMEGA Laser-Fusion Facility."

J. M. Soures, S. J. Loucks, R. L. McCrory, C. P. Verdon, A. Babushkin, R. E. Bahr, T. R. Boehly, R. Boni, D. K. Bradley, D. L. Brown, J. A. Delettrez, R. S. Craxton, W. R. Donaldson, R. Epstein, R. Gram, D. R. Harding, P. A. Jaanimagi, S. D. Jacobs, K. Kearney, R. L. Keck, J. H. Kelly, T. J. Kessler, R. L. Kremens, J. P. Knauer, S. A. Letzring, D. J. Lonobile, L. D. Lund, F. J. Marshall, P. W. McKenty, D. D. Meyerhofer, S. F. B. Morse, A. Okishev, S. Papernov, G. Pien, W. Seka, R. W. Short, M. J. Shoup, III, M. D. Skeldon, S. Skupsky, A. W. Schmid, D. J. Smith, S. Swales, M. D. Wittman, and B. Yaakobi, "The Role of the Laboratory for Laser Energetics in the National Ignition Facility Project."

S. G. Lukishova, S. V. Belyaev, K. S. Lebedev, E. A. Magulariya, A. W. Schmid, and N. V. Malimonenko, "Nonlinear Bleaching in the Selective Reflection of Nonabsorbing Chiral-Nematic Liquid-Crystal Thin Films," 16th International Liquid Crystal Conference, Kent, OH, 24–28 June 1996.